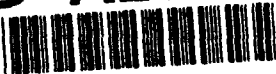


AD-A283 960

Dist: A

50014 ①

		TION PAGE		Form Approved OMB No. 0705-0188	
1. A		940630		3. REPORT TYPE AND DATES COVERED Final Report 901215 to 940630	
4. TITLE AND SUBTITLE High Temperature Stability of Binary Microstructures Derived from Liquid Precursors				5. FUNDING NUMBERS AFOSR 91-0125 2306/BS	
6. AUTHOR(S) Fred F. Lange				8. PERFORMING ORGANIZATION REPORT NUMBER AFOSR-IR- 94 0522	
7. PERFORMING ORGANIZATION NAME(S) AND ADDRESS(ES) Materials Department College of Engineering University of California Santa Barbara, CA 93106-5050				10. SPONSORING/MONITORING AGENCY REPORT NUMBER AFOSR - 91-0125	
9. SPONSORING/MONITORING AGENCY NAME(S) AND ADDRESS(ES) Dr. Alexander Pechenik/NC AFOSR/NC 110 Duncan Avenue, Suite B115 BOLLING AFB DC 20332-0001 NC					
11. SUPPLEMENTARY NOTES					
12A. DISTRIBUTION/AVAILABILITY STATEMENT Approved for public release, distribution unlimited A				12B. DISTRIBUTION CODE	
13. ABSTRACT (Maximum 200 words) This program has emphasized two topics: 1) the crystallization of metastable, solid-solution structures, their partitioning into equilibrium structures and compositions, and the role of the metastable phase and its partitioning on forming unique, nanometer microstructures important to the mechanics of structural ceramics and their composites, and 2) the formation of single crystal thin films via spin coating single crystal substrates with solution precursors. Results for the first topic are new, namely, the discovery that diffusion limited crystallization concepts used in rapid solidification directly applies to precursors that crystallize at low temperatures during heating. This discovery is significant because solid-solutions can be greatly extended relative to high temperature synthesis and processing routes where equilibrium conditions are rapidly achieved and solid-solutions can be severely limited. Extension of solid-solution fields (and thus defect chemistries) in compositional space is important to synthesize new materials with optical and electronic properties controlled by defect chemistry and/or metastable compositions. Results for the second topic have shown that single crystal thin films can be formed on single crystal substrates with spin-on liquid precursors despite large differences in lattice parameters and/or crystal structures. Several mechanisms have been identified for the growth of single crystal thin films which are very different to the well known vapor phase epitaxy mechanisms. The significance of the second topic is that single crystal (or poly-variant single crystal) thin films of nearly any inorganic material can be produced on any non-reactive (thermodynamically or kinetically) single crystal substrate, despite crystal structure differences between the film and substrate materials. Processing of multi-layer and/or embedded strip line architectures are possible using liquid precursor spin-on techniques for new device technologies.					
14. SUBJECT TERMS High Temperature, Binary Microstructures, Liquid Precursors				15. NUMBER OF PAGES 98	
17. SECURITY CLASSIFICATION OF REPORT Unclassified				18. SECURITY CLASSIFICATION OF THIS PAGE Unclassified	
19. SECURITY CLASSIFICATION OF ABSTRACT Unclassified				20. LIMITATION OF ABSTRACT	

94-28362



9998

DTC QUANTITY INDICATED 1

94 8 3 1 1 3 8

# High Temperature Stability of Binary Microstructures Derived From Liquid Precursors

Contract AFOSR-91-0125

## Final Report

June 30, 1994

From

Materials Department  
College of Engineering  
University of California  
Santa Barbara, CA 93106

Accession For	
NTIS CRA&I	<input checked="checked" type="checkbox"/>
DTIC TAB	<input type="checkbox"/>
Unannounced	<input type="checkbox"/>
Justification .....	
By .....	
Distribution /	
Availability Codes	
Dist	Avail and / or Special
A-1	

Principal Investigator: Fred F. Lange

## 1. Background

This program has emphasized two topics: 1) the crystallization of metastable, solid-solution structures, their partitioning into equilibrium structures and compositions, and the role of the metastable phase and its partitioning on forming unique, nanometer microstructures important to the mechanics of structural ceramics and their composites, and 2) the formation of single crystal thin films via spin coating single crystal substrates with solution precursors. Results for the first topic are new, namely, the discovery that diffusion limited crystallization concepts used in rapid solidification directly applies to precursors that crystallize at low temperatures during heating. This discovery is significant because solid-solutions can be greatly extended relative to high temperature synthesis and processing routes where equilibrium conditions are rapidly achieved and solid-solutions can be severely limited. Extension of solid-solution fields (and thus defect chemistries) in compositional space is important to synthesize new materials with optical and electronic properties controlled by defect chemistry and/or metastable compositions. Results for the second topic have shown that single crystal thin films can be formed on single crystal substrates with spin-on liquid precursors despite large differences in lattice parameters and/or crystal structures. Several mechanisms have been identified for the growth of single crystal thin films which are very different to the well know vapor phase epitaxy mechanisms. The significance of the second topic is that single crystal (or poly-variant single crystal) thin films of nearly any inorganic material can be produced on any non-reactive (thermodynamically or kinetically) single crystal substrate, despite crystal structure differences between the film and substrate materials. Processing of multi-layer and/or embedded strip line architectures are possible using liquid precursor spin-on techniques for new device technologies.

## 2. Summary of Research for Last Period

### 2.1 Kinetic Limited Crystallization and Phase Partitioning with Solution Precursors

#### 2.1.1 Development of Nano-Composite Microstructures in $\text{ZrO}_2\text{-Al}_2\text{O}_3$ Via the Solution Precursor Method, Mari Lou Balmer, Fred F. Lange, Vikram Jayaram and Carlos G. Levi

##### Technical Report No. 10

**Abstract:** Aqueous mixtures of zirconium acetate and aluminum nitrate were pyrolyzed and crystallized to form a metastable solid solution,  $\text{Zr}_{1-x}\text{Al}_x\text{O}_{2-x/2}$  ( $x \leq 0.57$ ). The initial, metastable phase partitions at higher temperatures to form two metastable, viz.,  $t\text{-(Zr,Al)O}_2 + \gamma\text{-(Al,Zr)}_2\text{O}_3$  with a nano-scale microstructure. The microstructural observations associated with the  $\gamma \rightarrow \alpha\text{-Al}_2\text{O}_3$  phase transformation in the  $t\text{-ZrO}_2$  matrix are reported for compositions containing 10, 20 and 40 mol%  $\text{Al}_2\text{O}_3$ . During this phase transformation the  $\alpha\text{-Al}_2\text{O}_3$  grains take the form of a colony of irregular, plate-like grains, all with a common crystallographic orientation, containing  $\text{ZrO}_2$  inclusions and separated by  $\text{ZrO}_2$  grains. At lower volume fractions of  $\text{Al}_2\text{O}_3$ , the colonies coarsen to single, irregular plates, surrounded by polycrystalline  $\text{ZrO}_2$ . The heat treatment condition also controls the microstructure. Interpenetrating microstructures produced at high volume fractions of  $\text{Al}_2\text{O}_3$  exhibit very little grain growth for periods up to 24h at 1400 °C.

#### 2.1.2 $^{27}\text{Al}$ NMR of $\text{Zr}_{(1-x)}\text{Al}_x\text{O}_{(2-x/2)}$ Solid Solutions Synthesized with Solution Precursors, Mari Lou Balmer, Nandini Das, Hellmut Eckert, and Fred F. Lange

##### Technical Report No. 11

**Abstract:** The local environment of the aluminum atoms in a series of metastable  $\text{Zr}_{(1-x)}\text{Al}_x\text{O}_{(2-x/2)}$  solid solutions ( $0.08 \leq x \leq 0.57$ ), prepared by diffusion-limited crystallization of amorphous precursors, has been determined by  $^{27}\text{Al}$  magic-angle spinning (MAS) NMR. Results show the existence of aluminum in 4-, 5-, and 6-fold coordination in both the amorphous and crystalline states. While the relative amounts of each type of coordination show no compositional dependence in the amorphous state, the results for the crystalline materials show a systematic decrease in the average Al coordination number with increasing Al content. Comparisons of MAS NMR results between pure  $\text{Al}_2\text{O}_3$  precursors and  $\text{Zr}_{(1-x)}\text{Al}_x\text{O}_{(2-x/2)}$  solid solutions processed under the same conditions show a profound effect of zirconia on the coordination environment of the Al atom. Both a random distribution model and a model which assumes small scale clustering of Al ions are considered to explain the trends in the type of Al coordination as a function of composition.

## 2.2 Single Crystal Thin Films via Solution Precursor Routes

### 2.2.1 Epitaxial Growth of $\text{PbTiO}_3$ Thin Films on $\{100\}$ $\text{SrTiO}_3$ from Solution Precursors Andreas Seifert, Fred F. Lange and James S. Speck

#### Technical Report No. 12

**Abstract:** A mixed alkoxide liquid precursor was used to form epitaxial  $\text{PbTiO}_3$  thin films by spin-coating on cubic (001)  $\text{SrTiO}_3$  substrates. The films were heat-treated at temperatures between 380°C and 800°C. X-ray diffraction, atomic force microscopy, scanning and transmission electron microscopy were used to characterize the microstructure of the films and to evaluate the epitaxial phenomena. At ~ 400°C a polycrystalline, metastable fluorite crystallizes from the amorphous, pyrolyzed precursor. At slightly higher temperatures (~420°C) the thermodynamically stable perovskite phase epitaxially nucleates at the film/substrate interface. A small number of epitaxial grains grows through the film toward the surface, consuming the nanometer-size, polycrystalline grains with the fluorite structure. Grain coarsening leads to a reduction in mosaic spread during further heating. Pores that concurrently coarsen, produce a pitted surface as they disappear from within the epitaxied film. At 800°C a dense, epitaxied  $\text{PbTiO}_3$  film with a smooth surface is observed. Parameters governing the formation of a- and c-domains are discussed as well as the small tilts of the domain axes away from the substrate normal.

# **High Temperature Stability of Binary Microstructures Derived From Liquid Precursors**

**Contract AFOSR-91-0125**

**Technical Report No. 10**

## **Development of Nano-Composite Microstructures in $\text{ZrO}_2$ - $\text{Al}_2\text{O}_3$ Via the Solution Precursor Method**

**Mari Lou Balmer <sup>a</sup>, Fred F. Lange, Vikram Jayaram <sup>b</sup> and  
Carlos G. Levi**

**Materials Department  
College of Engineering  
University of California, Santa Barbara  
Santa Barbara, CA 93106**

**Final Report June 30, 1994**

**Principal Investigator: Fred F. Lange 805 893 8248**

**Submitted to the Journal of the American Ceramic Society**

---

<sup>a</sup> Now at Battelle Pacific Northwest Laboratories, Richland, WA

<sup>b</sup> Visiting from the Indian Institute of Science, Bangalore, India

# Development of Nano-Composite Microstructures in $\text{ZrO}_2\text{-Al}_2\text{O}_3$ Via the Solution Precursor Method

Mari Lou Balmer <sup>a</sup>, Fred F. Lange, Vikram Jayaram <sup>b</sup> and Carlos G. Levi

Materials Department  
College of Engineering  
University of California, Santa Barbara  
Santa Barbara, CA 93106

## Abstract

Aqueous mixtures of zirconium acetate and aluminum nitrate were pyrolyzed and crystallized to form a metastable solid solution,  $\text{Zr}_{1-x}\text{Al}_x\text{O}_{2-x/2}$  ( $x \leq 0.57$ ). The initial, metastable phase partitions at higher temperatures to form two metastable phases, viz.,  $t\text{-(Zr,Al)O}_2 + \gamma\text{-(Al,Zr)}_2\text{O}_3$  with a nano-scale microstructure. The microstructural observations associated with the  $\gamma \rightarrow \alpha\text{-Al}_2\text{O}_3$  phase transformation in the  $t\text{-ZrO}_2$  matrix are reported for compositions containing 10, 20, and 40 mol%  $\text{Al}_2\text{O}_3$ . During this phase transformation the  $\alpha\text{-Al}_2\text{O}_3$  grains take the form of a colony of irregular, plate-like grains, all with a common crystallographic orientation. The plates contain  $\text{ZrO}_2$  inclusions and are separated by  $\text{ZrO}_2$  grains. The volume fraction of  $\text{Al}_2\text{O}_3$  and the heat treatment conditions influence the final microstructure. At lower volume fractions of  $\text{Al}_2\text{O}_3$ , the colonies coarsen to single, irregular plates, surrounded by polycrystalline  $\text{ZrO}_2$ . Interpenetrating microstructures produced at high volume fractions of  $\text{Al}_2\text{O}_3$  exhibit very little grain growth for periods up to 24 hours at 1400 °C.

---

<sup>a</sup> Now at Battelle Pacific Northwest Laboratories, Richland, WA

<sup>b</sup> Visiting from the Indian Institute of Science, Bangalore, India

## 1. Introduction

Previous studies by the authors <sup>1</sup> have shown that aqueous mixtures of zirconium acetate and aluminum nitrate pyrolyze and crystallize to a metastable, single phase solid-solution over the compositional range described by  $t\text{-Zr}_{(1-x)}\text{Al}_x\text{O}_{(2-x/2)}$  ( $x \leq 0.57$ ). When  $0.57 < x < 0.67$ , the crystallization temperature is sufficiently high so that crystallization and partitioning occur concurrently, resulting in two phase  $t\text{-(Zr,Al)}_2 + \gamma\text{-(Al,Zr)}_2\text{O}_3$ . In all cases an amorphous solid is first produced during pyrolysis, and crystallization to the metastable phase occurs at a temperature which increases with the  $\text{Al}_2\text{O}_3$  content. The grain size of the initial, metastable crystalline phase is  $\approx 3$  to 5 nm. When diffusional constraints are relieved by heating to higher temperatures or by holding at temperature for long periods, all single phase crystalline compositions ( $\leq 40$  mol%  $\text{Al}_2\text{O}_3$ ) partition into a nano-crystalline (grain size = 20-100 nm), two-phase material,  $t\text{-(Zr,Al)}\text{O}_2 + \gamma\text{-(Al,Zr)}_2\text{O}_3$ . These two-phase microstructures were shown to be extremely stable at temperatures  $\leq 1000^\circ\text{C}$ , maintaining grain sizes of less than 100 nm for up to 100 hours at  $1000^\circ\text{C}$ . After long periods at high temperatures ( $\geq 1300^\circ\text{C}$ ) all compositions reach their equilibrium phase assemblage,  $t\text{-ZrO}_2 + \alpha\text{-Al}_2\text{O}_3$ .<sup>c</sup>

The present paper describes the microstructural development that occurs when metastable, nano-crystalline  $\gamma\text{-Al}_2\text{O}_3$  transforms to  $\alpha\text{-Al}_2\text{O}_3$  within the zirconia matrix. It will be shown that unique two phase microstructures are produced, which are stable at high temperatures. The microstructural features of these composite materials may be desirable for producing materials with potentially interesting mechanical properties.

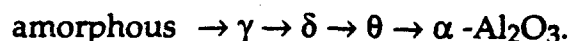
In order to better understand the  $\gamma \rightarrow \alpha\text{-Al}_2\text{O}_3$  transformation in a  $\text{ZrO}_2$  matrix, it is first convenient to review the phase transitions that are known to occur

---

<sup>c</sup> Some  $t\text{-ZrO}_2$  grains transform to  $m\text{-ZrO}_2$  on cooling



in single phase  $\text{Al}_2\text{O}_3$ . It is well known that there are a number of metastable polymorphs of aluminum oxide which exist in addition to the thermodynamically stable  $\alpha\text{-Al}_2\text{O}_3$ . The most commonly reported transformation sequence is:<sup>2-5</sup>



The crystal structures of these common polymorphs are:  $\gamma^d$  (cubic spinel),  $\delta$  (orthorhombic)<sup>6</sup>,  $\theta$  (monoclinic), and  $\alpha$  (rhombohedral). The oxygen ions are in a cubic close packed (ccp) arrangement in the  $\gamma$ ,  $\delta$ , and  $\theta$  structures and in a hexagonal close packed (hcp) arrangement in the  $\alpha$  structure. Cation ordering within the ccp based structures gives rise to the different metastable polymorphs. The initial alumina polymorph and the transformation sequence has been reported to depend on the precursor chemistry and the characterization technique.<sup>2,3,5</sup> Precise characterization of the metastable phases is often difficult due to the fact that many of these phases produce broad x-ray diffraction spectra (XRD) which are distinguished from one another by weak diffraction peaks.

## 2. Experimental Procedure

Compositions were prepared as aqueous solutions containing aluminum nitrate hydrate <sup>e</sup> and zirconium acetate <sup>f</sup>, such that the pyrolyzed product would contain 10, 20 and 40 mol%  $\text{Al}_2\text{O}_3$ . To avoid the selective crystallization of the aluminum nitrate during solvent removal, the solutions were atomized onto a Teflon coated, aluminum substrate at 250 °C to yield a powder which was amorphous by x-ray diffraction analysis (XRD) and electron diffraction. The powders were then heated in a furnace at a rate of 10 °C/min., or upquenched to

<sup>d</sup> Also identified in the literature as  $\eta$

<sup>e</sup> Fisher Scientific reagent grade aluminum nitrate hydrate

<sup>f</sup> Chemical composition by ICP mass spectroscopy in ref #7

temperatures ranging from 900 °C to 1400 °C. Upquenching was achieved by placing the spray pyrolyzed powder into a Pt crucible then thrusting it into a furnace at the desired temperature. Most specimens were held at temperature for 1 hour.

Scanning electron microscopy (SEM)<sup>g</sup>, and transmission electron microscopy (TEM)<sup>h</sup> were used to determine grain size and to characterize microstructural development as a function of heat treatment conditions. SEM powder specimens were prepared by bonding the composite flakes to an aluminum SEM specimen holder with graphite dag, then sputter coating with gold. Powder specimens were prepared for observation in the TEM by placing large, thin particles between two carbon coated Cu grids and ion milling for 1 hour in Ar (gun settings: 5 kV, 1 mA). Chemical analysis of powders was performed using energy dispersive spectroscopy (EDS)<sup>i</sup> in the TEM with a 100 nm diameter probe.

### 3. Results

Backscattered electron images of specimens containing 10 mol% Al<sub>2</sub>O<sub>3</sub> heated to 1100 , 1200 , 1300 , and 1400 °C at 10°C/min. and held for one hour are shown in Fig. 1. At temperatures  $\leq 1100$  °C, the two phase (t-(Zr,Al)O<sub>2</sub> +  $\gamma$ -(Al,Zr)<sub>2</sub>O<sub>3</sub>) microstructure appears homogeneous by TEM and SEM with a grain size ranging between 40-100 nm (Fig. 1a). At 1200 °C, SEM and TEM images reveal that large (2 to 4  $\mu$ m), but thin, plate-like Al<sub>2</sub>O<sub>3</sub>-rich grains (darker areas in Fig. 1b) containing nanometer ZrO<sub>2</sub> inclusions have formed within a matrix of ZrO<sub>2</sub> grains (lighter areas). As shown in Fig. 1, the plate-like grains are always irregular, and can appear as two or more closely spaced plates (Fig. 1b) that coarsen into single, irregular plates at higher temperatures (Fig. 1c and d). As the plate-like alumina grains are formed, the ZrO<sub>2</sub> microstructure becomes bimodal; ZrO<sub>2</sub> grains immediately surrounding

---

<sup>g</sup> JEOL 840-A SEM

<sup>h</sup> JEOL 2000FX

<sup>i</sup> Link Analytical

the  $\text{Al}_2\text{O}_3$  plates are generally larger ( $\approx 0.5 \mu\text{m}$ ) relative to those elsewhere ( $\approx 0.1 \mu\text{m}$ ). The  $\text{ZrO}_2$  matrix exhibits considerable grain coarsening ( $0.5$  to  $3 \mu\text{m}$ ) when heated to  $1300^\circ\text{C}/1\text{h}$ , but does not significantly change between  $1300^\circ\text{C}/1\text{h}$  and  $1400^\circ\text{C}/1\text{h}$ . After heating at  $1400^\circ\text{C}/1\text{h}$ , no significant microstructural changes were observed for an additional  $1400^\circ\text{C}/24\text{h}$  heat treatment.

The effects of thermal history on the microstructural development is illustrated by comparing Figs. 1 and 2. This comparison shows that the formation of the  $\text{Al}_2\text{O}_3$ -rich phase with a plate-like morphology is retarded by upquenching relative to slow heating. Figure 2 shows backscattered electron images of a specimen containing 10 mol%  $\text{Al}_2\text{O}_3$  which was upquenched to  $1300^\circ\text{C}$  and held for one and two hours. After one hour at  $1300^\circ\text{C}$ , only a few  $\text{Al}_2\text{O}_3$  plates are observed; however, a larger number of plates are seen after 2 hours (Fig. 2b). The number density of  $\text{Al}_2\text{O}_3$  plates is approximately the same for the unquenched specimen held for 2 hr at  $1300^\circ\text{C}$  and the specimen slowly heated to  $1300^\circ\text{C}$  and then cooled, however, the  $\text{ZrO}_2$  grain size is smaller for the upquenched sample even though it spent a longer period at  $1300^\circ\text{C}$  ( $0.1 \mu\text{m}$  to  $0.5 \mu\text{m}$  for upquenching, Fig. 2a, vs.  $0.5 \mu\text{m}$  to  $3.0 \mu\text{m}$  for  $10^\circ\text{C}/\text{min}$  to  $1300^\circ\text{C}/1\text{h}$ , Fig. 1c). Consistent with observations of slowly heated specimens, Fig. 2b shows that the  $\text{ZrO}_2$  grains adjacent to the growing  $\text{Al}_2\text{O}_3$  plates are much larger relative to those in the bulk matrix.

Backscattered electron images of samples containing 40 mol%  $\text{Al}_2\text{O}_3$ , heat treated at  $1200^\circ\text{C}$ ,  $1300^\circ\text{C}$ , and  $1400^\circ\text{C}$  for one hour, are shown in Figure 3. For heat treatments between  $1000^\circ\text{C}/1\text{h}$  and  $1200^\circ\text{C}/1\text{h}$ , TEM observations show that the two phases present are  $\gamma\text{-Al}_2\text{O}_3$  (grain size  $5 \text{ nm}$  to  $15 \text{ nm}$ ) and  $t\text{-ZrO}_2$  (grain size  $10 \text{ nm}$  to  $50 \text{ nm}$ ). At  $1200^\circ\text{C}/1\text{h}$  the grain size of the  $\text{ZrO}_2$  matrix appears to slightly increase ( $20 \text{ nm}$  to  $100 \text{ nm}$ ) and a uniformly distributed second phase of  $\gamma\text{-Al}_2\text{O}_3$  can be clearly identified with the TEM. In addition, the nucleation and growth of  $\alpha\text{-Al}_2\text{O}_3$  colonies, each with plate-like morphologies is observed. In contrast to the

composition containing 10 mol%  $\text{Al}_2\text{O}_3$ , where only two or three closely spaced plates are observed at lower temperatures, the composition containing 40 mol%  $\text{Al}_2\text{O}_3$  forms large colonies of closely spaced plates during the nucleation of  $\alpha\text{-Al}_2\text{O}_3$ .  $\alpha\text{-Al}_2\text{O}_3$  regions with an apparent spherulitic morphology (Fig. 3a, lower right hand corner) are occasionally observed, and are believed to correspond to colonies which are viewed normal to the plane of the plates. At 1300 °C/1h, the separation distance between the individual plates within each colony increases. This space becomes occupied by well developed  $\text{ZrO}_2$  grains ( $\approx 100$  nm). In addition, by 1300 °C/1h, the individual colonies of  $\alpha\text{-Al}_2\text{O}_3$  plate-like grains have grown large enough to impinge on one another. Larger (0.5 to 1  $\mu\text{m}$ )  $\text{ZrO}_2$  grains are observed between the colonies. Some coarsening is observed for specimens heated to 1400 °C/1h (Fig 3c), however, the morphology does not change. No significant change in microstructure is observed after a 24 h period at 1400 °C relative to the 1400 °C/1h heat treatment. Figure 3 also illustrates that, at comparable temperatures, the  $\text{ZrO}_2$  grain size is smaller relative the material containing 10 mol%  $\text{Al}_2\text{O}_3$  shown in Fig 1.

Compositions containing 40 mol%  $\text{Al}_2\text{O}_3$  which were upquenched to 1300 °C and held for different periods had similar microstructures to those which were conventionally heated with the exception that the onset of the plate formation was delayed. Selected area diffraction in the TEM of the upquenched (5 min. at 1300 °C) specimen showed the existence of  $t\text{-ZrO}_2 + \gamma\text{-Al}_2\text{O}_3$ . Specimens which were upquenched to 1300 °C/1h exhibited a uniform microstructure with a grain size of  $\approx 0.1$   $\mu\text{m}$  to 0.3  $\mu\text{m}$  (similar to that shown in Fig 1a) with infrequent areas where colonies of plates had begun to form (Fig. 4). The microstructure within the plates is similar to the slowly heated specimen, however, the regions devoid of platelets exhibit a much finer grain size (0.1 vs. 1  $\mu\text{m}$ ) relative to the slowly heated specimen.

The microstructure of  $\text{ZrO}_2\text{-Al}_2\text{O}_3$  containing 20 mol%  $\text{Al}_2\text{O}_3$  was examined by SEM at 1100, 1200, and 1300 °C. The temperature at which the  $\text{Al}_2\text{O}_3$ -rich platelets appeared (1200 °C) was identical to 10 and 40 mol%  $\text{Al}_2\text{O}_3$  compositions. Microstructures for the 20 mol% composition appear intermediate relative to those shown and discussed above. Namely, the number of plate-like layers within a given  $\alpha\text{-Al}_2\text{O}_3$  colony and their spacing at 1300 °C is intermediate relative to those shown in Figs. 1c and 3b.

Selected area diffraction patterns (SAD) were used to identify the structure of the plate-like  $\text{Al}_2\text{O}_3$ -rich grains (96 to 99 mol%  $\text{Al}_2\text{O}_3$  by EDS) in 10 and 40 mol% compositions. For both compositions heat treated at 1300°C/1h, electron diffraction revealed that the plates are  $\alpha\text{-Al}_2\text{O}_3$  with the 'c' axis perpendicular to the face of the plate. An occasional plate (<1%) had the  $\beta\text{-Al}_2\text{O}_3$  structure presumably due to Na contamination either in the precursor or the heating environment. The  $\beta\text{-Al}_2\text{O}_3$  plates could easily be distinguished from the  $\alpha\text{-Al}_2\text{O}_3$  plates by the much larger spacing between lattice fringes when viewed at high resolution. The early stages of  $\alpha\text{-Al}_2\text{O}_3$  formation were observed in TEM with a 40 mol%  $\text{Al}_2\text{O}_3$  composition heat treated to 1200°C. Figures 5a and 5b show low and high magnification dark field images of a region of  $\alpha\text{-Al}_2\text{O}_3$  growing in a  $t\text{-ZrO}_2 + \gamma\text{-Al}_2\text{O}_3$  matrix. Figure 5c shows a high magnification image of the matrix material. The diffraction pattern in Fig. 5d shows the  $\alpha\text{-Al}_2\text{O}_3$  pattern (  $[2\ 0\ \bar{2}\ 1]$  zone axis) along with the ring pattern for polycrystalline  $t\text{-ZrO}_2 + \gamma\text{-Al}_2\text{O}_3$ . In this early stage of growth, the transforming  $\alpha\text{-Al}_2\text{O}_3$  colonies exhibit irregular, branching growth, which evolves into the plate-like morphology. The  $\text{ZrO}_2$  grains are uniformly dispersed within the transforming  $\alpha\text{-Al}_2\text{O}_3$ . The matrix material shown in Fig. 5c is an interpenetrating mixture of  $(t+m)\text{-ZrO}_2$  (darker) +  $\gamma\text{-Al}_2\text{O}_3$  (lighter) without any transformed  $\alpha\text{-Al}_2\text{O}_3$  regions. (Monoclinic (m)  $\text{ZrO}_2$  grains are assumed to transform from  $t\text{-ZrO}_2$  during cooling.) Figure 6a shows a TEM micrograph of the cross section of a colony of  $\alpha\text{-Al}_2\text{O}_3$

(lighter regions) platelets growing into the polycrystalline matrix (heat treated 1300°C/1hr). The brightest region in the center of the photo is a crack. Dark field imaging and electron diffraction has shown that all of the plate-like grains within each colony have the same crystallographic orientation with minor 'tilts' along the length. Figure 6b shows a TEM micrograph of a cross section of two  $\alpha$ -Al<sub>2</sub>O<sub>3</sub> platelets with similar orientation growing into a matrix of polycrystalline t-ZrO<sub>2</sub> +  $\gamma$ -Al<sub>2</sub>O<sub>3</sub> in a 40 mol% Al<sub>2</sub>O<sub>3</sub> specimen heat treated to 1300 °C/1hr. An area where the plate thickened in the [0001] direction can clearly be seen in the middle of the brighter plate and nano-meter ZrO<sub>2</sub> grains are observed to be entrapped within the Al<sub>2</sub>O<sub>3</sub> single crystal plates. A combination of electron diffraction and dark field imaging verified that the platelets were the same single crystal of  $\alpha$ -Al<sub>2</sub>O<sub>3</sub> along the entire length. Although an occasional orientation relationship was observed between a ZrO<sub>2</sub> grain and an  $\alpha$ -Al<sub>2</sub>O<sub>3</sub> plate, the vast majority of ZrO<sub>2</sub> grains adjoining the plates did not show any preferred orientation relation.

#### 4. Discussion

Colonies of lamellar  $\alpha$ -Al<sub>2</sub>O<sub>3</sub>, are observed to form when  $\gamma$ -(Al,Zr)<sub>2</sub>O<sub>3</sub> transforms to  $\alpha$ -Al<sub>2</sub>O<sub>3</sub> within a two phase, t-(Zr,Al)O<sub>2</sub> and  $\gamma$ -(Al,Zr)<sub>2</sub>O<sub>3</sub>, matrix. The plates are not perfectly planar, contain embedded ZrO<sub>2</sub> inclusions and are separated by ZrO<sub>2</sub> grains. All Al<sub>2</sub>O<sub>3</sub> grains within a single colony have the same crystallographic orientation, and thus appear to grow from a single nucleus.

The  $\gamma$ -(Al,Zr)<sub>2</sub>O<sub>3</sub> to  $\alpha$ -Al<sub>2</sub>O<sub>3</sub> transformation temperature observed in the present work is at least 100 °C higher than reported for by others <sup>7,8</sup> for pure Al<sub>2</sub>O<sub>3</sub> precursors. The higher transformation temperature is presumably due to the need of the ZrO<sub>2</sub> in the metastable  $\gamma$ -(Al,Zr)<sub>2</sub>O<sub>3</sub> to partition during the transformation, viz., the equilibrium solubility of ZrO<sub>2</sub> in  $\alpha$ -Al<sub>2</sub>O<sub>3</sub> is very low.<sup>9</sup> Similar to the  $\gamma$  to  $\alpha$  transformation in pure Al<sub>2</sub>O<sub>3</sub> precursors,<sup>8</sup> the number density of growing nuclei

are very small. Namely, the distance between growing nuclei (or size of the colonies) are  $\approx 5 \mu\text{m}$ , or  $\approx 2$  orders of magnitude larger than the grain size of either phase in the metastable, two phase assemblage.

Although  $\text{Al}_2\text{O}_3$  is known to form plate-like crystals from the vapor state<sup>10</sup> and plate-like grains with relatively small aspect ratios during high temperature grain growth within dense, polycrystalline  $\text{Al}_2\text{O}_3$ ,<sup>11, 12</sup> the plate-like growth observed in the present work is much different. The major difference is that the growth of the  $\alpha\text{-Al}_2\text{O}_3$  grains occurs via a transformation ( $\gamma\text{-(Al,Zr)}_2\text{O}_3 \rightarrow \alpha\text{-Al}_2\text{O}_3 + \text{t-ZrO}_2$ ) within a dense, two phase polycrystalline matrix consisting of metastable  $\text{t-(Zr,Al)O}_2$  and  $\gamma\text{-(Al,Zr)}_2\text{O}_3$ . The formation of the plate-like grains is not observed during the  $\gamma$  to  $\alpha$  transformation in pure  $\text{Al}_2\text{O}_3$  precursors systems.<sup>8</sup> As shown by Dynys and Halloran,<sup>13</sup> the  $\gamma$  to  $\alpha$  transformation in pure  $\text{Al}_2\text{O}_3$  precursor systems can occur before the nanometer, polycrystalline  $\gamma$  matrix is fully dense. In this case, the boundary of the growing  $\alpha\text{-Al}_2\text{O}_3$  grains moves through the porous, nanometer, polycrystalline  $\gamma$  matrix to produce large, 'wormy'  $\alpha\text{-Al}_2\text{O}_3$  grains, viz.,  $\alpha\text{-Al}_2\text{O}_3$  grains with an embedded, connective porosity. In a similar manner, the growing  $\alpha\text{-Al}_2\text{O}_3$  grains that form within the  $\text{t-(Zr,Al)O}_2$  and  $\gamma\text{-(Al,Zr)}_2\text{O}_3$  matrix encompass the  $\text{ZrO}_2$  phase. Although entrapment of the  $\text{ZrO}_2$  phase suggests that the  $\alpha\text{-Al}_2\text{O}_3$  grains grow as a moving transformation front without much long range diffusion, the observation that enhanced growth of the  $\text{ZrO}_2$  grains surrounding the  $\alpha\text{-Al}_2\text{O}_3$  plates (Figs. 1b and 2) clearly shows that the plates grow via  $\text{Al}_2\text{O}_3$  diffusion from the surrounding matrix. That is, lateral redistribution of  $\text{Al}^{3+}$  in the  $\gamma\text{-(Al,Zr)}_2\text{O}_3$  phase must occur for the  $\alpha\text{-Al}_2\text{O}_3$  plates to grow, and for the  $\text{ZrO}_2$  grains to coarsen. The  $\alpha\text{-Al}_2\text{O}_3$  plates grow by a branching mechanism, where the extent of branching depends on the volume fraction of  $\text{Al}_2\text{O}_3$ , and the spacing between the plates is a function diffusion.

The growth of  $\alpha$ - $\text{Al}_2\text{O}_3$  as colonies of plate-like grains appears to be caused, in part, by the decrease in molar volume associated with the  $\gamma$  to  $\alpha$  transformation within the dense, two phase matrix. That is, large stresses can arise as a growing  $\alpha$ - $\text{Al}_2\text{O}_3$  ( $\rho=3.98$  g/cc) grain consumes  $\gamma$ - $\text{Al}_2\text{O}_3$  grains ( $\rho=3.65$  g/cc) within the surrounding matrix.<sup>14,15</sup> As detailed elsewhere,<sup>16</sup> when  $\alpha$ - $\text{Al}_2\text{O}_3$  grains grow with a plate-like morphology (c-axis parallel to the plate axis), the strain energy that arises during the transformation is reduced.

In conclusion, it can be seen that two phase microstructure, with nanometer sized grains can be produced from precursors that crystallize as one phase under kinetically limited conditions, then partition to equilibrium phases at higher temperatures. In the current case, one of the phases develops as colonies of plate-like grains. When the volume fraction of both phases is large, the higher temperature stability of the two phase microstructure can be attributed to the fact that both phases are interpenetrating and the growth of either requires long range diffusion.<sup>17-22</sup>

## 5. Conclusions

It is shown that partitioning of metastable  $\text{Zr}_{(1-x)}\text{Al}_x\text{O}_{(2-x/2)}$  containing 10, 20 and 40 mol%  $\text{Al}_2\text{O}_3$  yields unique nano-composite microstructures. Colonies of plate-like  $\alpha$ - $\text{Al}_2\text{O}_3$  grains grow during the  $\gamma \rightarrow \alpha$  phase transformation. The grain size and morphology of the partitioned phases depends on the relevant amounts of each component and the heat treatment conditions. Microstructures that develop from the final partitioned phases exhibit very little grain growth, and remain stable for extended periods at 1400 °C.

## Acknowledgment:



This work was supported by the Air Force Office of Scientific Research, under Contract No. AFOSR-91-0125. Support for C.G. Levi and V. Jayaram through grant DMR-89-15209 from the National Science Foundation is gratefully acknowledged.

## References

1. M.L. Balmer, F.F. Lange and C.G. Levi, "Metastable Phase Selection and Partitioning for  $Zr_{(1-x)}Al_xO_{(2-x/2)}$  Materials Synthesized with Liquid Precursors," submitted to *J. Am. Cer. Soc.*, Sept. 1993.
2. T. Sato, F. Ozawa, and S. Ikoma, "Thermal Decomposition of Aluminum Salts-Hydrates of the Chloride, Nitrate and Sulphate, and of Ammonium Alum," *J. Appl. Chem. Biotechnol.*, Vol. 28, pp. 811-22 (1978).
3. M. Kumagai, and G.L. Messing, "Controlled Transformation and Sintering of Boehmite Sol-Gel by  $\alpha$ - $Al_2O_3$  Seeding," *J. Am. Cer. Soc.*, Vol. 68 [9], pp 500-505 (1985).
4. L. Pach, R. Roy, and S. Komarneni, "Nucleation of Alpha Alumina in Boehmite Gel," *J. Mater. Res.*, Vol. 5, No. 2, pp. 278-85 (1990).
5. T. C. Chou and T.G. Neih, "Nucleation and Concurrent Anomalous Grain Growth of  $\alpha$ - $Al_2O_3$  During  $\gamma \rightarrow \alpha$  Phase Transformation," *J. Am. Cer. Soc.*, 74 [9], pp. 2270-79 (1991).
6. V. Jayaram and C.G. Levi, "The Structure of  $\delta$ -Alumina Evolved From the Melt and the  $\gamma \rightarrow \delta$  Transformation," *Acta. Metall.*, Vol. 37, No. 2, pp. 569-78 (1989).
7. W.E. Lee and K.P.D. Lagerlof, "Structural and Electron Diffraction Data for Sapphire ( $\alpha$ - $Al_2O_3$ )," *J. of Electron Microscopy Technique*, Vol. 2, pp. 247-258, 1985.

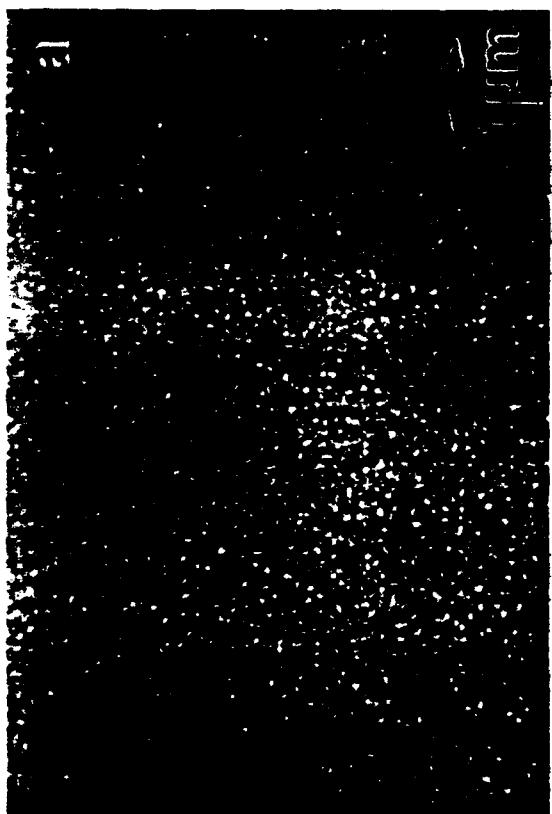
8. J.L. McArdle and G.L. Messing, "Seeding with  $\gamma$ -Alumina for Transformation and Microstructure Control in Boehmite-Derived  $\alpha$ -Alumina," *J. Am. Cer. Soc.*, Vol. 69 [5], pp. C98-C101 (1986).
9. M. J. Bannister, "Development of  $\text{SiO}_2$  Oxygen Sensor: Sub-Solidus Phase Equilibrium in the System  $\text{ZrO}_2\text{-Al}_2\text{O}_3\text{-Y}_2\text{O}_3$ ," *J. Aust. Ceram. Soc.* 18 [1], 6 (1982).
10. E.A.D. White, and J.D.C. Wood, "The Growth of Highly Perfect Alumina Platelets and Other Oxides by Solvent Vapour Transport," *J. Mat. Sci.*, Vol. 9, pp. 1999-2006 (1974).
11. A. Mocellin, and W.D. Kingery, "Microstructural Changes During Heat Treatment of Sintered  $\text{Al}_2\text{O}_3$ ," *J. Am. Cer. Soc.*, Vol. 56 [6], pp. 309-314 (1973).
12. H. Song, and R.L. Coble, "Origin and Growth Kinetics of Platelike Abnormal Grains in Liquid-Phase-Sintered Alumina," *J. Am. Cer. Soc.*, Vol. 73 [7], pp. 2077-85, (1990).
13. F.W. Dynys and J.W. Halloran, "Alpha Alumina Formation in Alumina-Derived Gamma Alumina," *J. Am. Cer. Soc.*, Vol. 65 [9], pp. 442-48 (1982).
14. W. E. Lee and K.P.D. Lagerlof, "Structural and Electron Diffraction Data for Sapphire," *J. Electron Microscopy Tech*, Vol 2, pp 247-258 (1985).
15. JCPDS Card No. 29-63 Revised from; Rooksby, X-ray Identification and Crystal Structures of Clay, London, p264, (1951).
16. W.E. Pompe, M.L. Balmer, and F.F. Lange, "Role of Elastic Constraints on Polymorphic Transformations in Oxide Ceramic Nano-composites Formed From Liquid Precursors," unpublished work to be submitted to *J. Am Cer. Soc.*
17. F.F. Lange and M.M. Hirlinger, "Hindrane of Grain Growth in  $\text{Al}_2\text{O}_3$  by  $\text{ZrO}_2$  Inclusions," *J. Am. Cer. Soc.*, Vol. 67 [3], pp. 164-68 (1984).

18. F.F. Lange and M.M. Hirlinger, "Grain Growth in Two-Phase Ceramics:  $\text{Al}_2\text{O}_3$  Inclusions in  $\text{ZrO}_2$ ," *J. Am. Cer. Soc.*, Vol. 70 [11], pp. 827-30 (1987).
19. S. Hori, R. Kurita, M. Yoshimura, and S. Somiya, "Suppressed Grain Growth in Final-Stage Sintering of  $\text{Al}_2\text{O}_3$  with Dispersed  $\text{ZrO}_2$  Particles," *J. Mat. Sci. Let.*, Vol. 4, pp. 1067-70 (1985).
20. J.B. Baldo and R.C. Bradt, "Grain Growth of the Lime and Periclase Phases in a Synthetic Doloma," *J Am. Cer. Soc.*, Vol. 71 [9], pp. 720-25 (1988).
21. J.W. Cahn "Stability, Microstructural Evolution, Grain Growth, and Coarsening in a Two-Dimensional Two-Phase Microstructure," *Acta. Metall. Mater.*, Vol. 39, No. 10, pp. 2189-99 (1991).
22. J.D. French, M.P. Harmer, H.M. Chan, and G.A. Miller, "Coarsening-Resistant Dual-Phase Interpenetrating Microstructures," *J. Am. Cer. Soc.*, Vol. 73 [8], pp. 2508-10 (1990).

### Figure Captions

- 1.) Backscattered electron images of partitioned  $\text{Zr}_{(1-x)}\text{Al}_x\text{O}_{(2-x/2)}$  containing the equivalent of 10 mol%  $\text{Al}_2\text{O}_3$  heat treated at (a) 1100 °C/1h, (b) 1200 °C/1h, (c) 1300 °C/1h and (d) 1400 °C/1h. Microstructure at 1100 °C/1h is two phase,  $\text{t-ZrO}_2 + \gamma\text{-Al}_2\text{O}_3$ ;  $\alpha\text{-Al}_2\text{O}_3$  nucleates at 1200 °C as stacked plates with embedded, nano-meter  $\text{ZrO}_2$  crystallites.
- 2.) Backscattered electron images of partitioned  $\text{Zr}_{(1-x)}\text{Al}_x\text{O}_{(2-x/2)}$  containing the equivalent of 10 mol%  $\text{Al}_2\text{O}_3$  upquenched to (a) 1300 °C/1h, (b) 1300 °C/2h.
- 3.) Backscattered electron images of partitioned  $\text{Zr}_{(1-x)}\text{Al}_x\text{O}_{(2-x/2)}$  containing the equivalent of 40 mol%  $\text{Al}_2\text{O}_3$  heat treated at (a) 1200 °C/1h, (b) 1300 °C/1h and

- (c) 1400 °C/1h. At 1200 °C  $\text{Al}_2\text{O}_3$ -rich regions grow as stacked plates within t- $\text{ZrO}_2 + \gamma\text{-Al}_2\text{O}_3$  two phase matrix.
- 4.) Backscattered electron image of partitioned  $\text{Zr}_{(1-x)}\text{Al}_x\text{O}_{(2-x/2)}$  containing the equivalent of 40 mol%  $\text{Al}_2\text{O}_3$  upquenched to 1300 °C/1h.
  - 5.) (a) Low and (b) high magnification dark field images of  $\alpha\text{-Al}_2\text{O}_3$  single crystalline regions, (c) matrix material (t+m)- $\text{ZrO}_2 + \gamma\text{-Al}_2\text{O}_3$ , and (d) diffraction pattern of the polycrystalline matrix (t+m)- $\text{ZrO}_2 + \gamma\text{-Al}_2\text{O}_3$ , and the single crystal  $\alpha\text{-Al}_2\text{O}_3$  in 40 mol%  $\text{Al}_2\text{O}_3$  heat treated (10 °C/min) to 1200°C/1h.
  - 6.) TEM micrograph of (a) a stack of  $\alpha\text{-Al}_2\text{O}_3$  platelets and (b) the tip of two  $\alpha\text{-Al}_2\text{O}_3$  platelets growing into a polycrystalline (t+m)- $\text{ZrO}_2 + \gamma\text{-Al}_2\text{O}_3$  matrix in a partitioned  $\text{Zr}_{(1-x)}\text{Al}_x\text{O}_{(2-x/2)}$  containing the equivalent of 40 mol%  $\text{Al}_2\text{O}_3$  heat treated (10 °C/min) to 1300 °C/1hr. Platelets within a stack have the same crystallographic orientation.



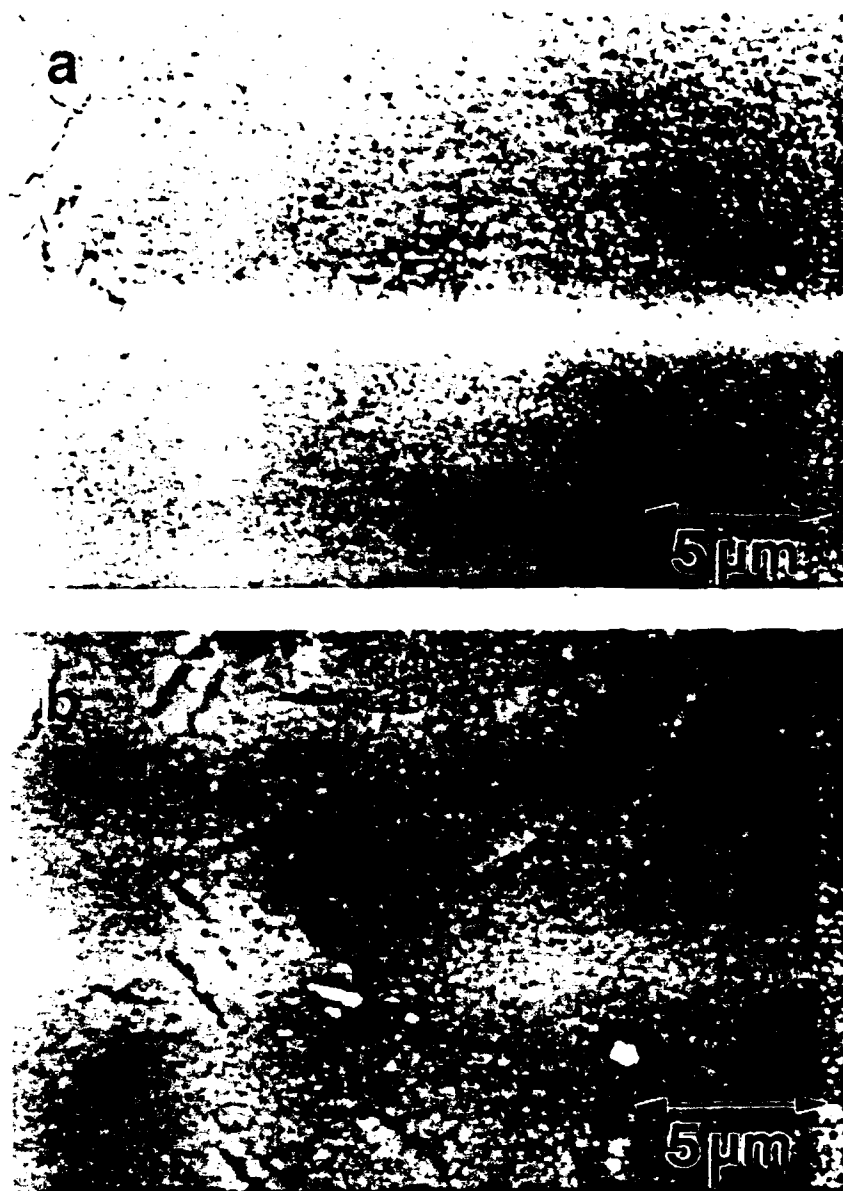


Figure 2

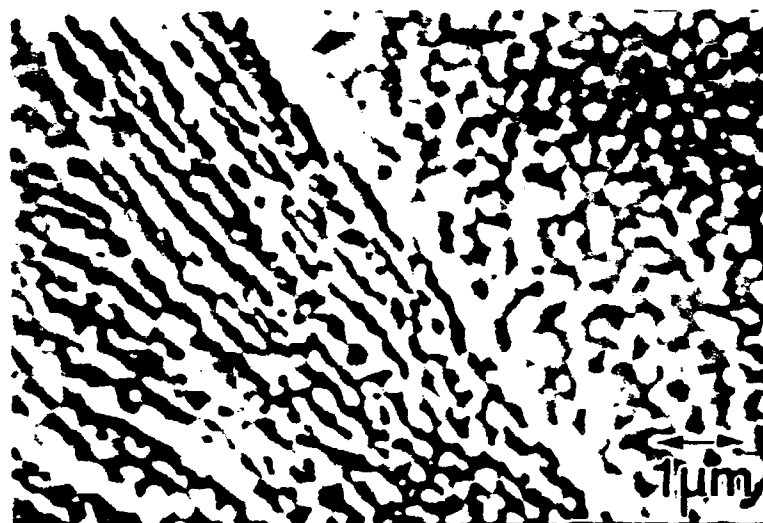
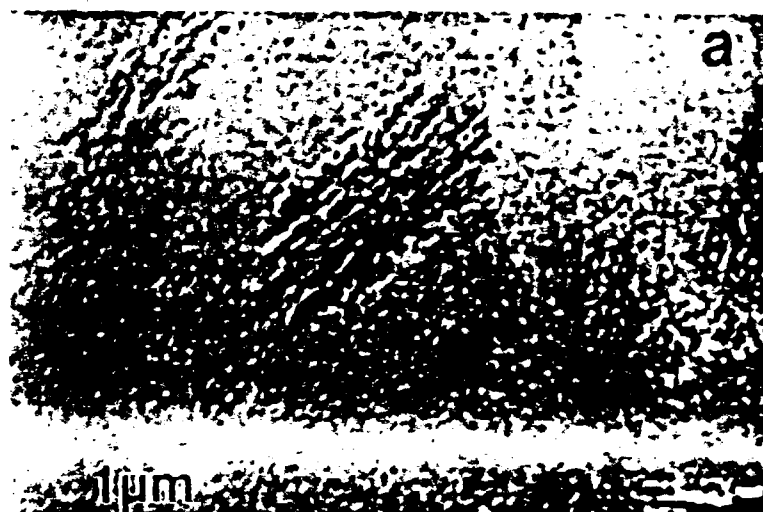




Figure 4

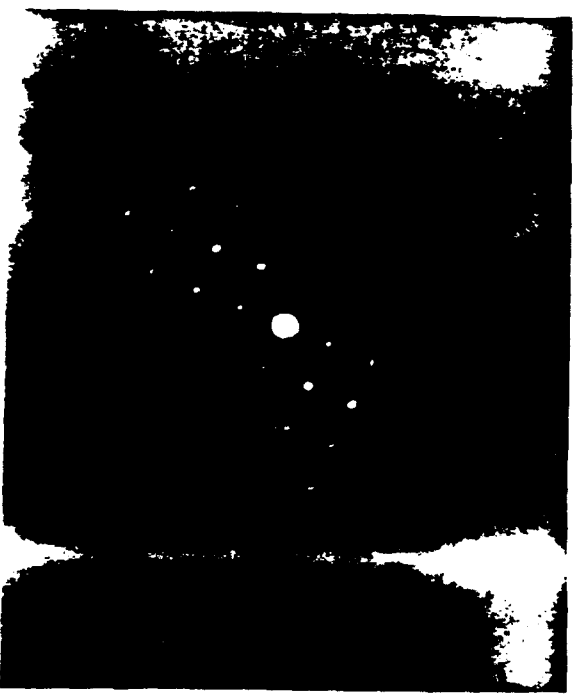




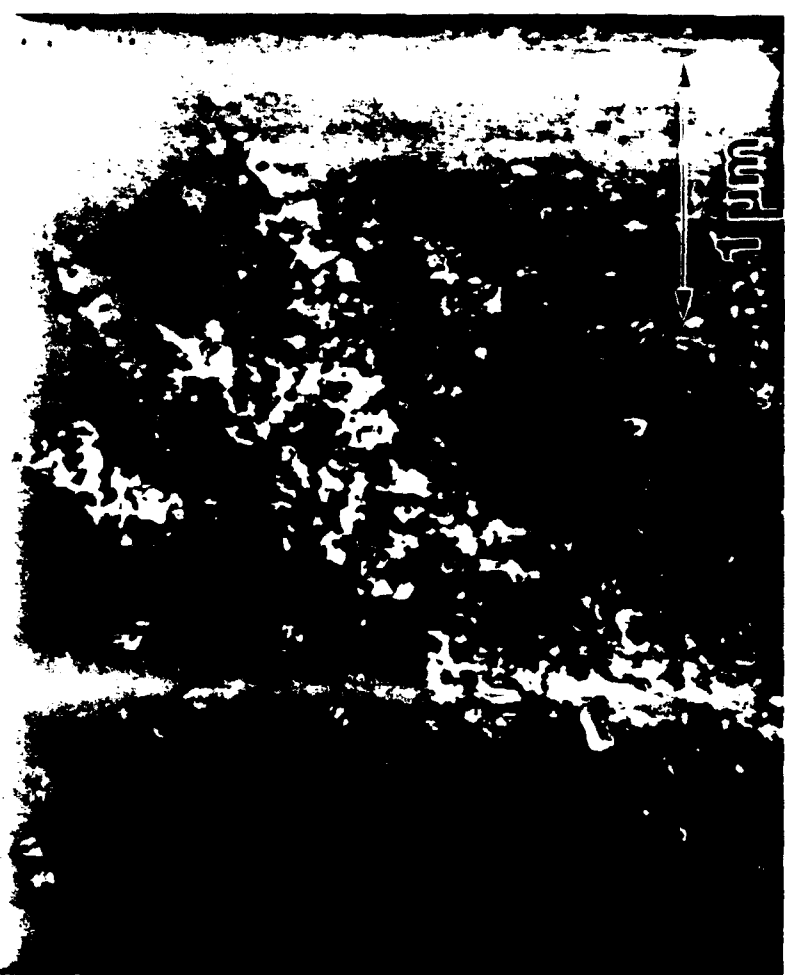
a)



c)



d)



b)

a)



b)

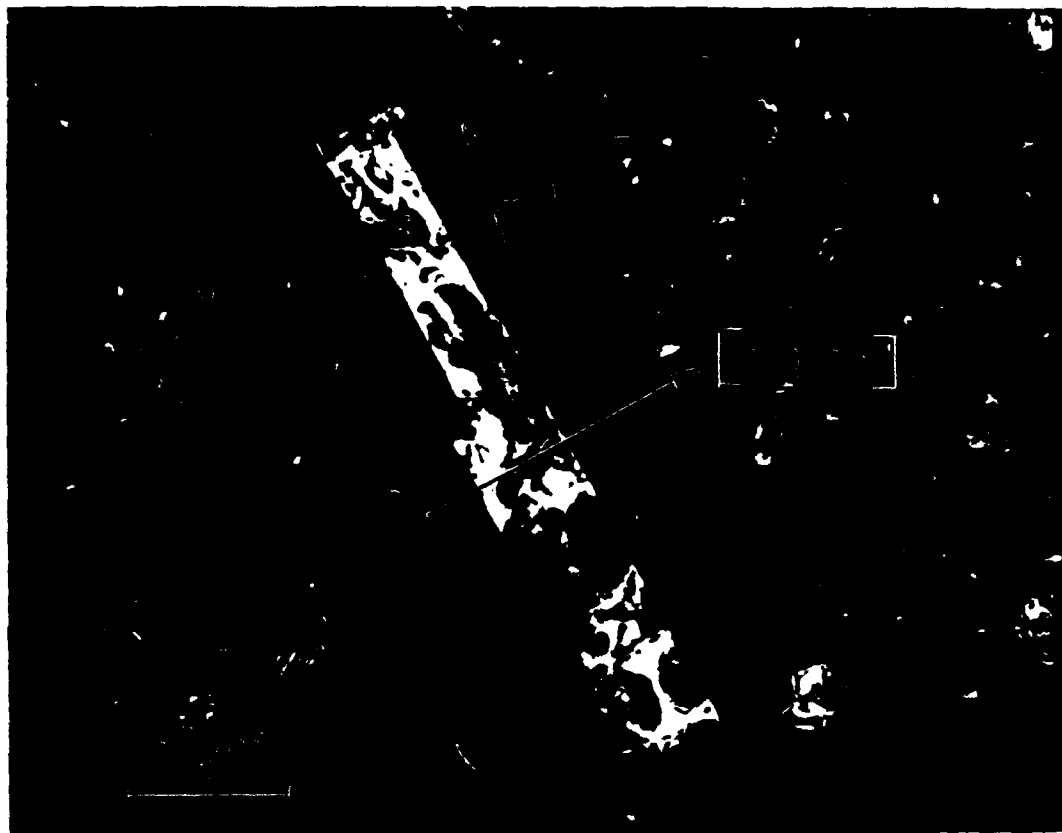


Figure 6

**High Temperature Stability of Binary Microstructures  
Derived From Liquid Precursors**

**Contract AFOSR-91-0125**

**Technical Report No.11**

**$^{27}\text{Al}$  NMR of  $\text{Zr}_{(1-x)}\text{Al}_x\text{O}_{(2-x/2)}$  Solid  
Solutions Synthesized  
with Solution Precursors**

**Mari Lou Balmer, Nandini Das, Hellmut Eckert,  
and Fred F. Lange**

**Materials Department  
College of Engineering  
University of California  
Santa Barbara, CA 93106**

**Final Report, June 30, 1994**

**Principal Investigator: Fred F. Lange 805 893 8248**

**Submitted to the Journal of the American Ceramic Society**

# **$^{27}\text{Al}$ NMR of $\text{Zr}_{(1-x)}\text{Al}_x\text{O}_{(2-x/2)}$ Solid Solutions Synthesized with Solution Precursors**

Mari Lou Balmer, Fred F. Lange,  
Materials Department  
College of Engineering

Nandini Das, and Hellmut Eckert  
Chemistry Department

University of California Santa Barbara  
Santa Barbara, CA 93106

## **Abstract**

The local environment of the aluminum atoms in a series of metastable  $\text{Zr}_{(1-x)}\text{Al}_x\text{O}_{(2-x/2)}$  solid solutions ( $0.08 \leq x \leq 0.57$ ), prepared by diffusion-limited crystallization of amorphous precursors, has been determined by  $^{27}\text{Al}$  magic-angle spinning (MAS) NMR. Results show the existence of aluminum in 4-, 5-, and 6-fold coordination in both the amorphous and crystalline states. While the relative amounts of each type of coordination show no compositional dependence in the amorphous state, the results for the crystalline materials show a systematic decrease in the average Al coordination number with increasing Al content. Comparisons of MAS NMR results between pure  $\text{Al}_2\text{O}_3$  precursors and  $\text{Zr}_{(1-x)}\text{Al}_x\text{O}_{(2-x/2)}$  solid solutions processed under the same conditions show a profound effect of zirconia on the coordination environment of the Al atom. Both a random distribution model and a model which assumes small scale clustering of Al ions are considered to explain the trends in the type of Al coordination as a function of composition.

## 1.0 Introduction

As shown in previous papers <sup>1,2</sup> a single phase solid solution with stoichiometry  $\text{Zr}_{(1-x)}\text{Al}_x\text{O}_{(2-x/2)}$  crystallizes from pyrolyzed amorphous precursor samples over the range  $0.08 \leq x \leq 0.58$  (4 to 40 mol%  $\text{Al}_2\text{O}_3$ ). Combined evidence from TEM, XRD and Raman spectroscopy shows that the  $\text{Zr}_{(1-x)}\text{Al}_x\text{O}_{(2-x/2)}$  system is single phase with the t- $\text{ZrO}_2$  structure. This large extension of the solubility range is unusual, since the equilibrium phase diagram predicts that even at high temperatures the maximum solubility of  $\text{Al}_2\text{O}_3$  in t- $\text{ZrO}_2$  is  $< 2$  mol%, which corresponds to a cation site substitution of  $x \approx 0.04$ .

In order to better understand the structural organization of these extended solid solutions it is helpful to examine the structure of each end member. t- $\text{ZrO}_2$  (S.G.  $\text{P4}_2/\text{nmc}$ ) is a distorted derivative of the fluorite structure (S.G.  $\text{Fm}3\text{m}$ ) shown in Figure 1. The zirconium ions occupy the corners and face centered unit cell positions and the oxygens occupy the tetrahedral sites. Each Zr is coordinated by eight oxygen ions, and each oxygen is coordinated by four Zr ions. Likewise, the oxygen ions have six oxygen next-nearest neighbors, and the Zr ions have 12 Zr next-nearest neighbors. As in the case with other trivalent and divalent ions ( $\text{Y}^{3+}$ ,  $\text{Ga}^{3+}$ ,  $\text{Ca}^{2+}$ ,  $\text{Mg}^{2+}$ ) which form solid solutions with  $\text{ZrO}_2$ , it is expected that  $\text{Al}^{3+}$  ions will substitute for  $\text{Zr}^{4+}$ . In order to maintain local charge balance, an oxygen vacancy must be created for every two trivalent ions substituted for  $\text{Zr}^{4+}$ . The yttria structure, which results from replacing all the  $\text{Zr}^{4+}$  by  $\text{Y}^{3+}$  in  $\text{ZrO}_2$ , is body centered cubic (D53), and may be visualized as a defect fluorite derivative where 25% of the oxygen sites are vacant, but all the cations remain approximately in the same f.c.c. array. The difference in stoichiometry leads to displacements of the true ionic positions away from those occupied in the fluorite structure, and hence to a change in cation-oxygen coordination, from cubic in  $\text{ZrO}_2$  to octahedral in  $\text{Y}_2\text{O}_3$ . In the case where yttria partially substitutes for Zr in the fluorite structure,  $\text{Y}^{3+}$  ions may be coordinated by 6 or 7 oxygens, depending on the number of closest  $\text{Y}^{3+}$  neighbors.

Aluminum has never been observed in 7-fold coordination with oxygen. In the crystal structures of the common polymorphs of  $\text{Al}_2\text{O}_3$ , the Al

ions are in tetrahedral and octahedral sites. The oxygen ions are in face centered cubic ( $\gamma$ ,  $\delta$ , and  $\Theta$ ), and hexagonal close packed ( $\alpha$ ) arrangements, and within each of these groups, the ordering of cations gives rise to the different polymorphs. The  $\gamma$ - $\text{Al}_2\text{O}_3$  structure, which is the first phase to partition from  $\text{Zr}_{(1-x)}\text{Al}_x\text{O}_{(2-x/2)}$  solid solutions, possesses a spinel-like structure. The Al ions are randomly distributed such that 10% of the tetrahedral sites and 46.7% of the octahedral sites are filled.<sup>3</sup>

The local environment of the Al ion (i.e. the Al-O coordination) can be determined with  $^{27}\text{Al}$  magic angle spinning nuclear magnetic resonance (MAS NMR). MAS NMR studies on  $\text{Al}_2\text{O}_3$  formed from various precursors have shown the existence of Al-O in 5-fold, as well as 4- and 6-fold coordinations. The relative amounts of each type of coordination varied depending on the starting materials, and as a function of heat treatment temperature.<sup>4,5</sup> 5-coordinate Al species are also known to exist in several minerals and synthesized compounds such as andalusite, grandidierite, yoderite, augelite, senegalite,  $\text{AlPO}_4\text{-12}$ , and  $\text{AlPO}_4\text{-21}$ , and several organic complexes.<sup>6</sup>

## 2.0 Experimental

### 2.1 Sample Preparation and Characterization.

$\text{ZrO}_2\text{-Al}_2\text{O}_3$  mixtures containing the equivalent of 0, 4, 7, 10, 15, 20, 33, 40, and 50 mol%  $\text{Al}_2\text{O}_3$  ( $x = 0, 0.08\text{-}0.67$ ) after pyrolysis were fabricated from aqueous solutions of zirconium acetate and aluminum nitrate. As detailed in an earlier paper,<sup>1</sup> the solutions were spray pyrolyzed in order to maintain intimate mixing and avoid selective crystallization of aluminum nitrate. The precursor compositions were all heated at a rate of  $15^\circ\text{C}/\text{minute}$  to  $400^\circ\text{C}$  and held for one hour to ensure that decomposition was complete. Previous work<sup>1</sup> has shown that crystallization occurs at temperatures  $> 400^\circ\text{C}$ , thus the  $400^\circ\text{C}$  samples were amorphous. After the  $400^\circ\text{C}$  treatment, a portion of the different samples were 'upquenched' to a temperature just above the crystallization temperature, which systematically increases with  $\text{Al}_2\text{O}_3$  content.<sup>1</sup> The 'upquench' procedure consisted of placing an amorphous powder into a platinum crucible, inserting it into a furnace, pre-heated to the desired temperature, holding 5 minutes, then removing the sample into

ambient temperature. The phase selection as a function of composition and upquench temperature for the crystalline samples is reported in reference 1.

## 2.2 NMR Studies

$^{27}\text{Al}$  MAS NMR was performed at 78.3 and 130.3 MHz on General Electric GN-300 (7.05 T) and GN-500 (11.7 T) spectrometers equipped with probes from Doty Scientific. The following experimental parameters were used: pulse length =  $1\mu\text{s}$  ( $45^\circ$  solid flip angle), recycle delays 1 s, spinning speed = 8-10 kHz. Spin counting studies were carried out with weighed samples and  $\gamma\text{-Al}_2\text{O}_3$  as the quantitation standard. The results indicate that both in the amorphous and the crystalline samples the fraction of Al detected amounts to ca. 75-90% of the fraction of the Al atoms detected in  $\gamma\text{-Al}_2\text{O}_3$  with no evident compositional dependence. Standard spectrometer software was used to eliminate the  $^{27}\text{Al}$  probe background signal. Resonance shifts were obtained at 130.3 MHz relative to a 1M aqueous solution of aluminum nitrate.

## 3.0 Results

NMR spectra collected at 130.3 MHz for samples containing the equivalent of 4 and 40 mol%  $\text{Al}_2\text{O}_3$  ( $x = 0.08$  and  $0.57$ ) in the amorphous and crystalline states are summarized in Figure 2; for the crystalline samples, the whole compositional series is displayed in Figure 3. The spectra are characterized by three resonance maxima near 60, 30 and 0 ppm, which are assigned to aluminum sites in four-, five- and six-fold coordination with oxygen. These resonances are flanked by broad shoulders which comprise spinning sidebands and possibly lineshape components not narrowed under the present experimental conditions. The resonance positions measured for the 4-, 5-, and 6-coordinated aluminum species are not equal to the chemical shifts, because the field-dependent NMR studies show a contribution,  $\delta^{(2)}$ , due to second-order quadrupolar effects:

$$\delta_{\text{exp}} = \delta_{\text{iso}} + \delta^{(2)} \quad (1)$$

Second-order quadrupolar interactions also lead to substantial line-broadening effects in the MAS-NMR spectra of quadrupolar nuclei such as  $^{27}\text{Al}$ , and decrease with increasing field strength. Comparison of spectra collected at 78.3 and 130.3 MHz reveals substantially improved resolution at the higher field strength, indicating the dominance of second-order quadrupolar broadening effects on the MAS-NMR lineshapes. Due to this situation, the exact lineshapes for the individual Al(4), Al(5), and Al(6) sites are expected to deviate from the regular Gaussians usually observed in MAS-NMR. Therefore, it is impossible to deconvolute the overall MAS NMR spectra in terms of quantitatively reliable site populations. However, assuming that the MAS NMR lineshape parameters for Al(4), Al(5), and Al(6) do not change over the range of compositions studied, the compositional trends in these site populations (relative percentages) can be visualized as shown in Figure 4 using peak height measurements,  $P(x)$ .

$$P(x) = 100 \cdot I_x / (I_4 + I_5 + I_6) \quad (x = 4, 5, 6), \quad (2)$$

where  $I_4$ ,  $I_5$ , and  $I_6$  are the peak heights of the MAS NMR lineshape components assigned to the respective aluminum sites. While the parameters  $P(x)$  are not equal to these site populations, it is our working assumption that any compositional change in  $P(x)$  is due to a change in these site populations. Because the peak overlap is more pronounced lower field strengths, the relative percentages of the aluminum sites as determined by this procedure from the 78.3 MHz spectra are somewhat different from those determined at 130.3 MHz. For this reason, the analysis of the 130.3 MHz is preferred, and the results shown in Figures 5 and 6 are based on these high-field data. Regardless of the assumption, it is worth noting, that each data set produces the same compositional trend in the aluminum population distribution.

As shown in Figure 5, there is little evidence that in the amorphous samples the relative percentages of each type of Al coordination vary substantially over the range of 7-40 mol%  $\text{Al}_2\text{O}_3$ . Mixtures containing 4 mol%  $\text{Al}_2\text{O}_3$  appear to have more 6-coordinated Al, and less 5- and 4-coordinated Al than is observed at other compositions. Samples containing 50 mol%  $\text{Al}_2\text{O}_3$  exhibit anomalously large amounts of 5- and 4-coordinated Al, and low amounts of 6-coordinated Al. For 100%  $\text{Al}_2\text{O}_3$  in the amorphous



state, the fraction of 4-coordinated Al is consistent with that in most of the samples, however, the relative percentage of 5-coordinated Al sites is significantly lower than that found in most of the  $\text{Zr}_{(1-x)}\text{Al}_x\text{O}_{(2-x/2)}$  solid solutions. This difference clearly illustrates the effect of zirconia on the aluminum speciations in the amorphous state.

Figure 6 shows the changes in  $P(x)$  for 4-, 5-, and 6-coordinated Al as a function of Al content for crystalline  $\text{Zr}_{(1-x)}\text{Al}_x\text{O}_{(2-x/2)}$  upquenched to a temperature just above the crystallization temperature. It can be seen that for compositions with small Al contents, the Al ion is primarily in 5- and 6-fold coordination. With increasing Al content, the relative percentage of 4-fold coordinated Al sites increases, whereas the 5- and 6-fold coordinated Al sites decrease. Figure 6 reveals a systematic compositional trend in the population distribution of the various aluminum sites over the range  $4 \leq \text{mol\% Al}_2\text{O}_3 \leq 40$ . At 50 mol%  $\text{Al}_2\text{O}_3$  an anomalously large amount of 6-coordinated Al is observed. As shown previously<sup>1</sup>, the 50 mol%  $\text{Al}_2\text{O}_3$  composition is known to partition during crystallization, resulting in the formation of  $\gamma\text{-Al}_2\text{O}_3$ . This is reflected in the relatively large fractions of 4- and 6-coordinated Al. For a sample which is known to be  $\gamma\text{-Al}_2\text{O}_3$ ,  $P_4$  and  $P_6$  are measured as 78% and 22% respectively, as can be seen on Figure 6 for the 100%  $\text{Al}_2\text{O}_3$  composition.

It is important to note that the representation of the data in Figures 5 and 6 does not reflect the absolute quantities of each type of Al-O coordination. The absolute amounts of each component increase systematically with increasing  $\text{Al}_2\text{O}_3$  content in the solid solutions as expected. Overall, the quantity of each component increases as a function of Al content as measured by the peak intensities for amorphous and crystalline samples.

As shown previously<sup>1</sup>, the crystallization temperature of the amorphous, pyrolyzed precursor increases with Al content. Therefore, the compositions represented in Figures 3 and 6 had to be upquenched to successively higher temperatures in order to promote crystallization. In order to ensure that the trends in Al coordination are indeed an effect of composition and not of crystallization temperature, spray pyrolyzed samples of pure Al-nitrate precursor were fabricated and upquenched to temperatures close to those for the samples shown in Figure 6. The trend in the relative percentages of 4-, 5-, and 6-coordinated Al sites as a function of increasing upquench temperature for pure  $\text{Al}_2\text{O}_3$  is shown in Figure 7 (corresponding

$\text{Al}_2\text{O}_3$  contents for  $\text{Zr}(\text{Al})\text{O}_2$  upquenched to the same temperature are shown in parenthesis). The data shown in Figure 7 were collected at 78.3 MHz, however, the trend is expected to be the same at 130.3 MHz. The relative percentage of 4-coordinated Al is constant over the temperature range studied, while the fraction of 6-coordinated Al increases slightly at the expense of 5-coordinated Al atoms, as the crystallization temperature increases. Overall, the trend in these samples is comparable to that in the amorphous mixed  $\text{Zr}(\text{Al})\text{O}_2$  samples, but decidedly different from that seen in the crystallized  $\text{Zr}(\text{Al})\text{O}_2$  materials (Fig. 6). Thus, it is clear that the dramatic changes in the aluminum coordination distribution in the crystallized  $\text{Zr}(\text{Al})\text{O}_2$  materials is not simply an effect of annealing temperature, but specifically reflects the interactions between the zirconia and alumina constituents in the crystalline state.

Figure 8 shows the compositional dependence of the resonance shift, measured at 130.3 MHz, associated with the 6-coordinated Al sites. There is no apparent dependence of the peak shift on the  $\text{Al}_2\text{O}_3$  content for the glassy samples. However, the crystalline materials exhibit a monotonic downfield shift trend as a function of increasing  $\text{Al}_2\text{O}_3$  content from 1.0 ppm to 9.1 ppm, the latter being the value observed for 6-coordinated Al in pure  $\gamma\text{-Al}_2\text{O}_3$ . This indicates that the environment of 6-fold Al in  $\text{Zr}_{(1-x)}\text{Al}_x\text{O}_{(2-x/2)}$  solid solutions varies significantly from that in  $\gamma\text{-Al}_2\text{O}_3$  but approaches it with increasing Al content as expected.

Figure 9 summarizes the results of the spin counting studies. It can be seen that in all  $\text{Zr}_{(1-x)}\text{Al}_x\text{O}_{(2-x/2)}$  solid solutions, approximately 75-90% of the Al detected in  $\gamma\text{-Al}_2\text{O}_3$  is detected, regardless of exact composition. This suggests that if 7-fold Al is the portion which is undetected, the amount of 7-coordinated Al would be the same over the range of compositions of  $\text{Zr}_{(1-x)}\text{Al}_x\text{O}_{(2-x/2)}$  solid solutions, a rather unlikely scenario. An alternative explanation of the signal loss is the larger line width of the peaks associated with the Al(5) sites, compared to those of the Al(4) and Al(6) sites in  $\gamma\text{-Al}_2\text{O}_3$ . This may result in incomplete detection of the Al(5) species in the solid solutions where Al(5) is highly abundant. The broadening of the Al(5) line presumably arises from stronger quadrupolar interactions as compared to the other sites.

## 4.0 Discussion

It is obvious that the crystallization of  $\text{Zr}_{(1-x)}\text{Al}_x\text{O}_{(2-x/2)}$  from the amorphous precursor, as well as the amount of Al in solid solution, has a profound effect on the Al-O coordination. In order to explain observed trends in Al site populations, two scenarios will be considered: 1) The oxygen vacancies generated by the Al substitution are randomly distributed in the zirconia lattice, and 2) The substitution generates clusters of Al atoms, with Al next nearest neighbors, that are larger than those predicted by random distributions, and the Al-O coordinations at the interface between the Al clusters and the matrix are different than those in the center of the cluster.

### 4.1 Random Distributions

The case where the oxygen vacancies are randomly distributed represents one extreme scenario. It assumes that the amorphous pyrolyzed materials are intimately mixed, and that there is no redistribution of solute upon crystallization of  $\text{Zr}_{(1-x)}\text{Al}_x\text{O}_{(2-x/2)}$ . Since an oxygen vacancy must be created for every two  $\text{Al}^{3+}$  ions substituting for Zr, a random distribution of vacancies results in a non-random distribution of Al atoms, as local charge constraints mandate that each oxygen vacancy is next to two Al sites. For such a pseudo-random distribution, the average Al-O coordination number should decrease from 7 to 6 with increasing Al content, reflecting the increasing number  $n_{\text{Al}}$  of aluminum atoms with at least one Al next nearest neighbor. The dependence of the average Al coordination number as a function of  $n_{\text{Al}}$  is shown in Figure 10. As in the case of  $\text{Y}^{3+}$ -substituted zirconia, even with complete substitution of Al for Zr in the fluorite structure, the minimum average Al-O coordination number should be 6. The trends determined experimentally for the  $\text{Zr}_{(1-x)}\text{Al}_x\text{O}_{(2-x/2)}$  solid solutions show an overall decrease in the average coordination number as a function of Al content similar to the trend expected for random distributions. However, the presence of 4-, ( $x \geq 0.13$ ) and 5-fold Al sites in relatively large amounts and the apparent absence of 7-coordinate Al environments can not be explained by this model.

Due to the distorted local symmetry of a 7-fold coordinated Al-O environment, the question arises as to whether the corresponding  $^{27}\text{Al}$  NMR

signal might be broadened beyond detection due to strong second-order quadrupolar effects. The fact that approximately 75-90% of the total Al signal observed for pure  $\gamma$ -alumina is detected for all compositions ( $0.08 \leq x \leq 0.57$ ) suggests that if 7-coordinated Al is present, it does not exist in significantly larger quantities for the lower concentrations of Al, as would be expected from the random distribution model. However, the current experiments do not explicitly rule out the existence of 7-fold coordinated Al atoms. It is a reasonable conjecture that relaxations or distortions of the fluorite structure could occur in the presence of Al-vacancy-Al groups. The  $\text{Al}^{3+}$  near a vacancy may suffer small local distortions of its oxygen environment causing some Al-O distances to become larger than others. This could effectively reduce the Al coordination number, and thus may make a 7-fold environment appear like a 5- or 6-fold Al site in  $^{27}\text{Al}$  MAS NMR.

Another reason for the lower Al coordination numbers may be grain boundary or surface effects. As shown previously<sup>1</sup> by TEM, the initial particle size of upquenched  $\text{Zr}_{(1-x)}\text{Al}_x\text{O}_{(2-x/2)}$  is 3-5 nm. For these very small grain sizes, the grain boundary area becomes significantly large. The surface area per unit volume can be calculated using the simple equation:<sup>7</sup>

$$S_V = \frac{2}{G} \quad (3)$$

where  $S_V$  is surface area per unit volume (1/length) and  $G$  is the grain size (length). If we assume that the grain boundary is one unit cell thick ( $\approx 5 \text{ \AA}$ ), then for an average grain size of 3 nm, 32 vol% of the material resides on the grain boundaries. Likewise for an average grain size of 5 nm, 20 vol% of the material resides on the grain boundaries. Cations which reside on the surface or grain boundary, are expected to have a lower coordination than those in the bulk. Therefore, assuming a completely random distribution of vacancies, aluminum atoms expected to be in 7- and 6-coordination may actually occur in 6- and 5-fold coordination, respectively. Since 8-fold coordination is energetically favorable for Zr, Al ions may preferentially reside on the surface of these domains. Regardless of these assumptions, it is clear that the random model cannot explain the experimental presence of  $\text{Al}(4)$  species.

TEM and DTA analysis shows that the crystallization of  $\text{Zr}_{(1-x)}\text{Al}_x\text{O}_{(2-x/2)}$  solid solutions from the amorphous phase occurs slowly over a temperature range of  $\approx 100^\circ\text{C}$ . It is possible that in the upquenched samples prepared for NMR experiments, small regions may remain amorphous after the heat treatment. These amorphous regions are expected to have Al-O coordination distributions similar to the amorphous  $\text{Zr}(\text{Al})\text{O}_2$  samples shown in Figure 4 ( $P_4 \approx 0.2$ ,  $P_5 \approx 0.42$ , and  $P_6 \approx 0.38$ ). Since four coordinated Al cannot be explained by the random distribution model as discussed above, it might be associated exclusively with the residual amorphous phase. Al in 6- and 5-fold coordination may result from either the crystalline or amorphous phases. If the volume fraction of the amorphous phase increases with increasing Al content, then a trend in average coordination number similar to that seen in the experimental data could be envisioned. Based on this interpretation the solubility of alumina in zirconia might be significantly lower than previously imagined.

#### 4.2 Clustering of Second Phase

A second model can be considered where the Al ions form Al-O-Al bonded clusters larger than those predicted by random distributions. Since percolating clusters can be physically described as irregular branching strings, the Al-rich clusters will be modeled here using a rod-like geometry, with a large aspect ratio. It is expected that the Al ions at the surface of the rod will be affected by the neighboring  $\text{Zr}^{4+}$  ions, and will have higher Al-O coordination numbers than in the center of the rod where the structure has relaxed to one corresponding to amorphous  $\text{Al}_2\text{O}_3$ . The relative amounts of 4-, 5-, and 6-coordinated Al atoms in the center are estimated from experimental values for pure  $\text{Al}_2\text{O}_3$  upquenched to  $600^\circ\text{C} \leq T \leq 800^\circ\text{C}$ . The Al-atoms on the surface of the rod (with a thickness of  $1/2$  a unit cell) are assumed to be in only 5- and 6-fold coordination. At small cluster sizes where the surface to volume ratio ( $S/V$ ) is large, Al will be primarily in 5- and 6-fold coordination, but as the cluster size increases the relative amount of 4-fold Al is expected to increase. Figure 11 illustrates the expected trend in the Al coordination distribution for an initial aspect ratio  $(l/r) = 100/1$  as a function of increasing cluster size. The trend is similar to that seen in Figure 6 for the experimental results for  $0.08 \leq x \leq 0.57$ .

MAS NMR experimental observations which show a change in the relative percentages of each type of coordination upon crystallization, as well as the observed trend for the Al(6) resonance shifts in the crystalline  $\text{Zr}_{(1-x)}\text{Al}_x\text{O}_{(2-x/2)}$  solid solutions, preclude the existence of large areas (on the order the grain size) of amorphous material. Similarly, TEM observations<sup>1</sup> of the initial crystalline microstructure did not reveal any recognizable amorphous regions. The uncertainty in the ability to detect 7-coordinated Al atoms or the manner in which the latter might manifest themselves in MAS NMR, makes it difficult to differentiate reliably between both models. It is therefore not possible to determine the precise solubility limit of the fluorite structure for aluminum substituents. Evidence suggests that the samples examined consist of random solid solutions at the lowest mole fractions of Al (<10 mol%). This conclusion is based on the absence of Al(4) sites in such samples. With increasing Al content larger Al-rich clusters form, whose size is probably larger than the cluster size predicted by random distributions. Most likely these clusters exist as disordered regions within the individual crystallites or on their surfaces.

## 5.0 Conclusions

It has been shown by  $^{27}\text{Al}$  MAS NMR that in crystalline  $\text{Zr}_{(1-x)}\text{Al}_x\text{O}_{(2-x/2)}$  solid solutions prepared from amorphous precursors, the Al ions are in 4-, 5-, and 6-fold coordination with oxygen. The relative amount of Al(4) sites increases, whereas the relative amount of Al(5) and Al(6) decreases systematically with increasing Al content in the crystalline materials. This trend may in part reflect the overall decrease of average Al coordination number expected for a random distribution of vacancies. As the number of Al next nearest neighbors increases with increasing Al content, the average coordination number is expected to decrease. On the other hand, the experimental data, specifically the occurrence of 4-coordinated Al sites, can also be explained by the formation of  $\text{Al}_2\text{O}_3$  clusters larger than those predicted by random distributions. In the cluster model, the coordination of the atoms on the surface of the clusters is expected to be influenced by the neighboring Zr atoms, while the atoms in the center of the clusters have coordination distributions similar to amorphous alumina. Seven-fold coordinated Al was not identified in this study. While such a species may go

undetected due to strong second order quadrupolar broadening effects, the spin counting studies carried out here indicate that the fraction of undetected signal is independent of composition, contrary to what is expected for the concentration of Al(7) in a random distribution model. It is, however, quite possible that the local structure around such a 7-coordinate Al atom relaxes, resulting effectively in lower coordination numbers.

## 6.0 Acknowledgements

This work was supported by an AFOSR under Contract No. F49620-94-1-0229. This work also made use of MRL Central Facilities supported by the National Science Foundation under Award No. DMR-9123048.

## 7.0 References

1. M.L. Balmer, F.F. Lange, and C.G. Levi, "Phase Selection and Extended Solubility in  $\text{ZrO}_2\text{-Al}_2\text{O}_3$  Processed from Liquid Precursors," submitted to *J. Am. Cer. Soc.* June, 1993.
2. M.L. Balmer, F.F. Lange, V. Jayaram, and C.G. Levi, "Development of Nano-Composite Microstructures in  $\text{ZrO}_2\text{-Al}_2\text{O}_3$  Via the Solution Precursor Method," to be submitted to *J. Am. Cer. Soc.* 1994.
3. L.J. Alvarez, and J.F. Sanz, "Molecular Dynamics Study of the Structure of  $\gamma$ -Alumina," *Chem. Phys. Letters*, Vol. 192, Nos. 5,6, pp. 463-468, 15 May 1992.
4. T.E. Wood, A.R. Siedle, J.R. Hill, R.P. Skarjune, and C.J. Goodbrake, "Hydrolysis of Aluminum-Are All Gels Created Equal?," *Mat. Res. Soc. Symp. Proc.*, Vol. 180, pp. 97-116, 1992.
5. L.F. Nazar, G. Fu, and A.D. Bain, " $^{27}\text{Al}$  MAS NMR Studies of a New Polyoxyaluminum Cluster and its Selective Transformation to Five-coordinate Aluminum in the Solid State," *J. Chem. Soc., Chem. Commun.*, pp. 251-253, 1992.

6. L.B. Alemany and G.W. Kirker, "First Observation of 5-Coordinate Aluminum by MAS NMR in Well Characterized Solids," *J. Am. Chem. Soc.*, 108, pp. 6158-62 1986 and references sited therein.
7. E.E. Underwood, "Applications of Quantitative Metallography," from *Metals Handbook Vol. 8, Metallography, Structures, and Phase Diagrams*, Am. Soc. Metals, pp.37-47, 1973.



### Figure Captions

- Figure 1: Schematic representation of the fluorite structure with the anions defining the unit cell.
- Figure 2: 130.3 MHz  $^{27}\text{Al}$  MAS-NMR spectra for  $\text{Zr}_{1-x}\text{Al}_x\text{O}_{(2-x/2)}$  solid solutions containing 4 and 40 mol%  $\text{Al}_2\text{O}_3$  ( $x = 0.08$ , bottom, and 0.57, top).
- Figure 3: 130.3 MHz  $^{27}\text{Al}$  MAS-NMR spectra of crystalline solid solution samples in the zirconia-alumina system. The compositions (mole%  $\text{Al}_2\text{O}_3$ ) are indicated.
- Figure 4: Schematic of peak height measurement procedure from the  $^{27}\text{Al}$  MAS-NMR spectra.
- Figure 5: Relative percentages of 4-, 5-, and 6-fold coordinated Al as a function of Al content in amorphous  $\text{Zr}(\text{Al})\text{O}_2$  heat treated at 400 °C/1hr, measured from  $^{27}\text{Al}$  MAS-NMR spectra at 130.3 MHz.
- Figure 6: Relative percentages of 4-, 5-, and 6-fold coordinated Al as a function of Al content in crystalline  $\text{Zr}_{(1-x)}\text{Al}_x\text{O}_{(2-x/2)}$ , measured from  $^{27}\text{Al}$  MAS-NMR spectra at 130.3 MHz.
- Figure 7: Relative percentages of 4-, 5-, and 6-fold coordinated Al as a function of upquench temperature for  $\text{Al}_2\text{O}_3$  formed from spray pyrolyzed aluminum nitrate, measured from  $^{27}\text{Al}$  MAS-NMR spectra at 78.3 MHz.
- Figure 8: Resonance shift  $\pm 0.5$  ppm (vs. 1M aq.  $\text{Al}(\text{NO}_3)_3$  solution) of the 6-fold coordinated Al peak as a function of equivalent  $\text{Al}_2\text{O}_3$  content in amorphous and crystalline mixtures, measured from  $^{27}\text{Al}$  MAS-NMR spectra at 130.3 MHz.

- Figure 9:  $^{27}\text{Al}$  MAS NMR signal intensity at 130.3 MHz relative to that measured in crystalline  $\gamma\text{-Al}_2\text{O}_3$  as a function of equivalent  $\text{Al}_2\text{O}_3$  content in amorphous and crystalline mixtures. The error in this measurement is estimated at  $\pm 5\%$ .
- Figure 10: Expected average Al coordination number in the fluorite structure as a function of  $n_{\text{Al}}$ , the number of Al atoms contained in alumina clusters with Al next nearest neighbors.
- Figure 11: Predicted relative percentages of 4-, 5-, and 6-fold coordinated Al as a function of increasing cluster volume. Clusters have a rod-like geometry where the center of the cluster contains Al in 4-, 5-, and 6-fold coordination in the same quantities as amorphous  $\text{Al}_2\text{O}_3$ , and the surface contains only 5- and 6- coordinated Al.

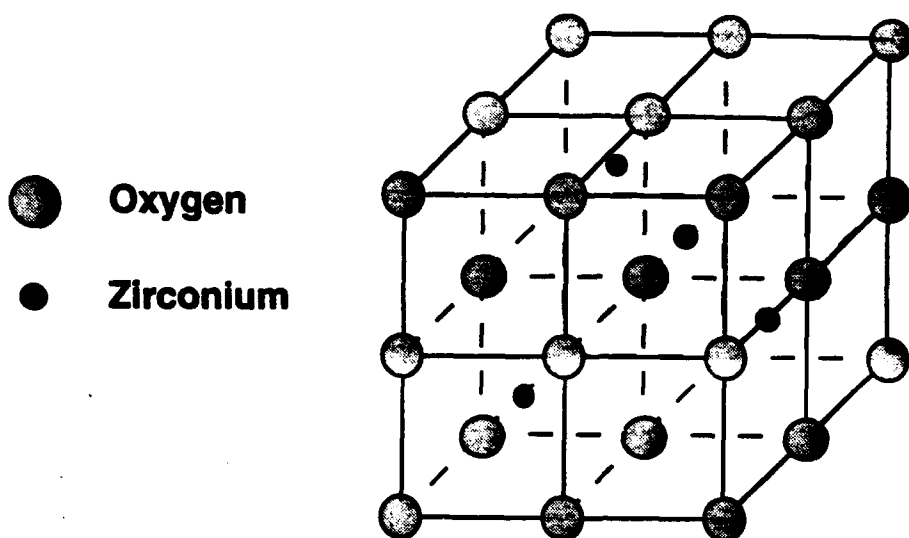


Figure 1

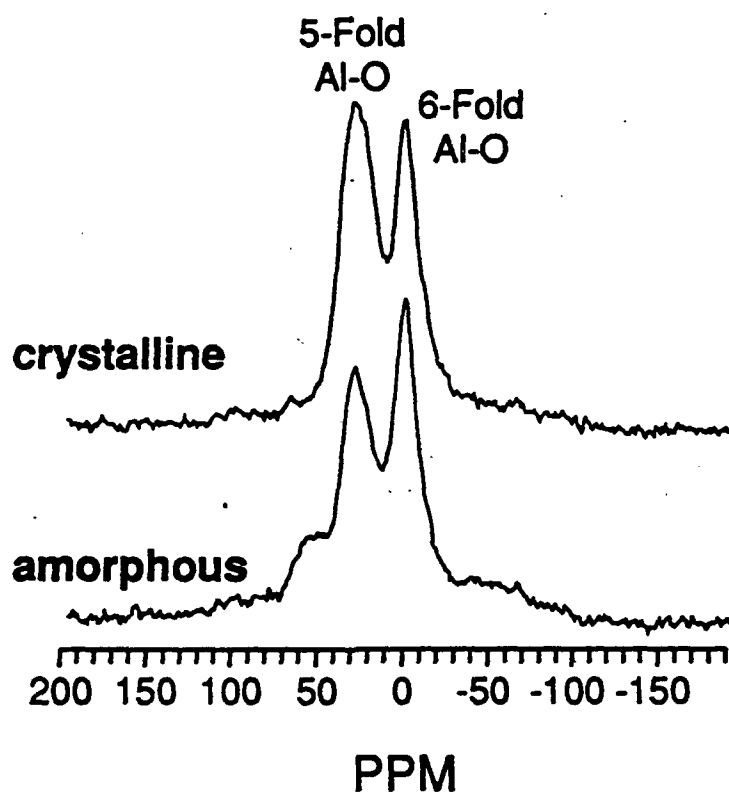
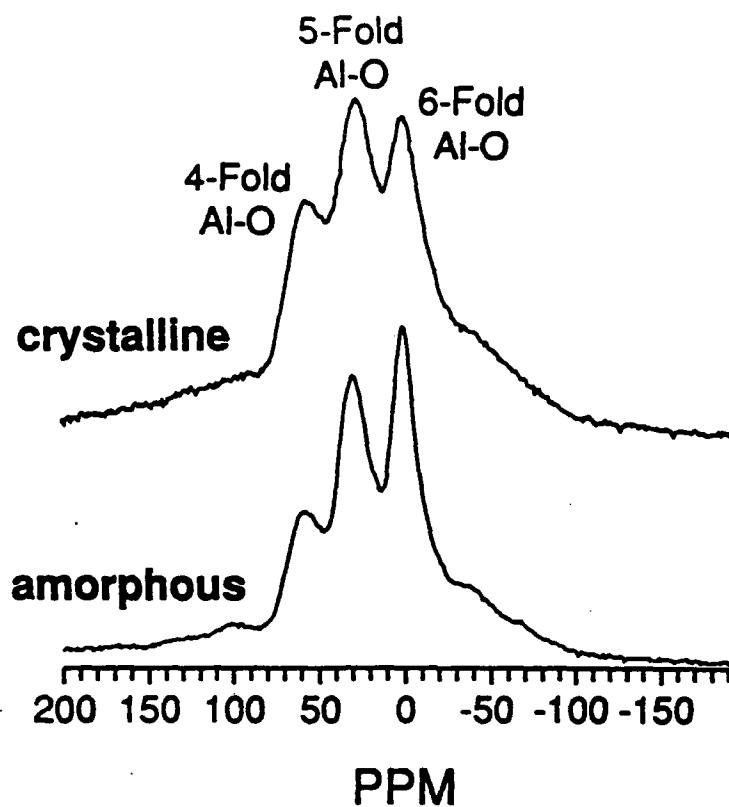


Figure 2

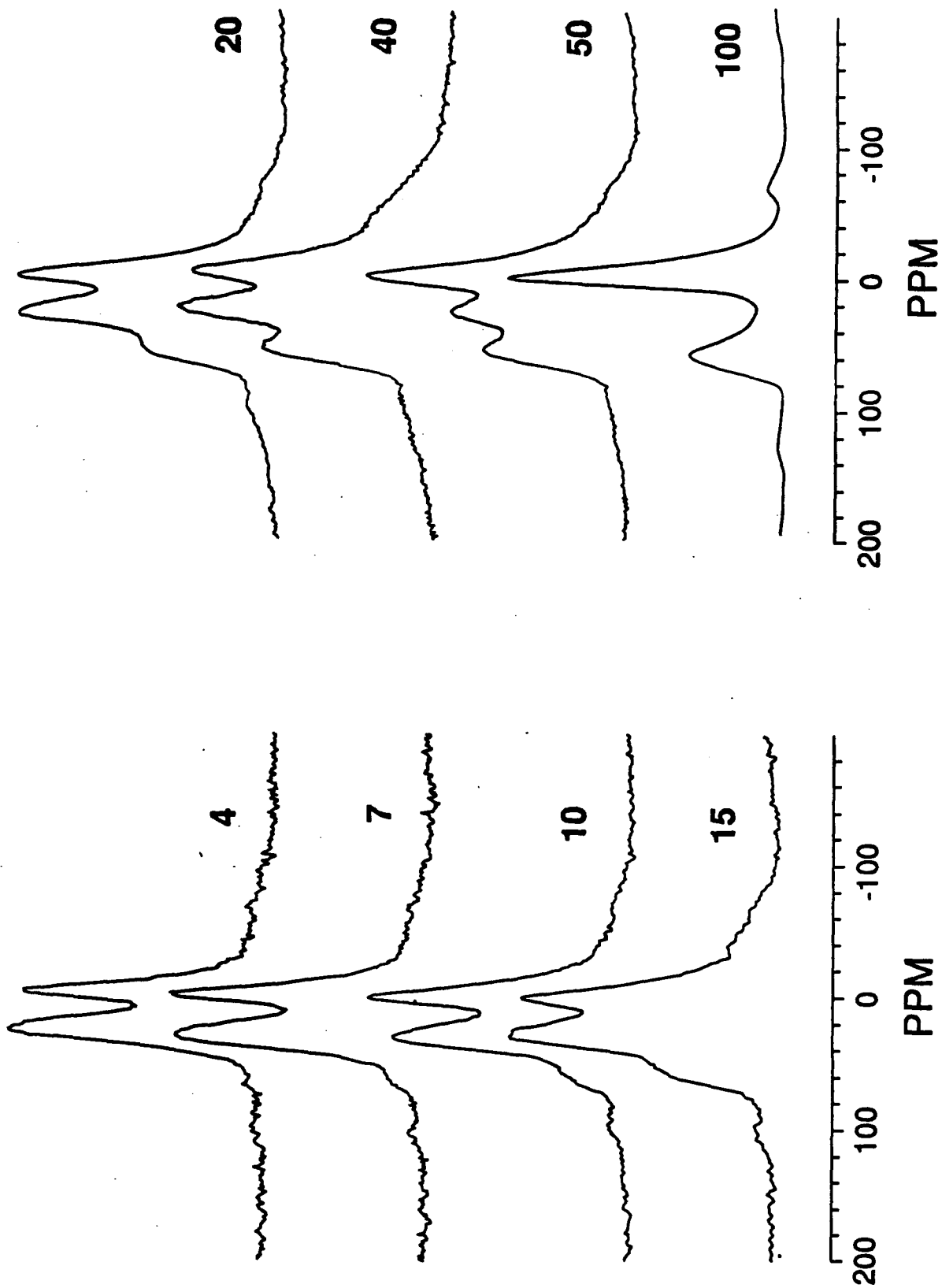


Figure 3

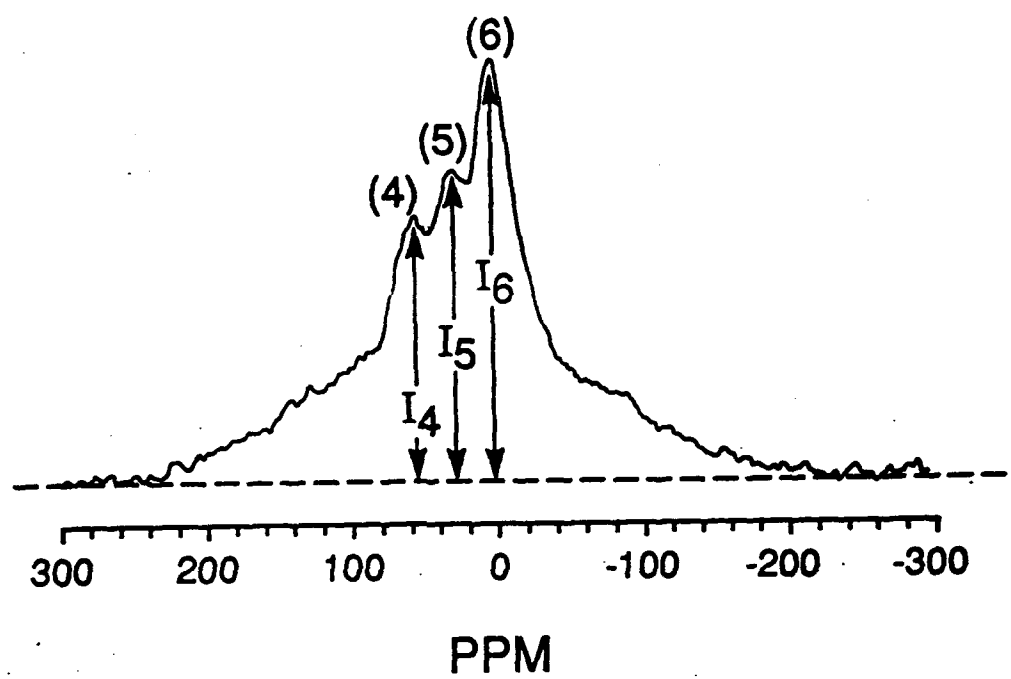


Figure 4

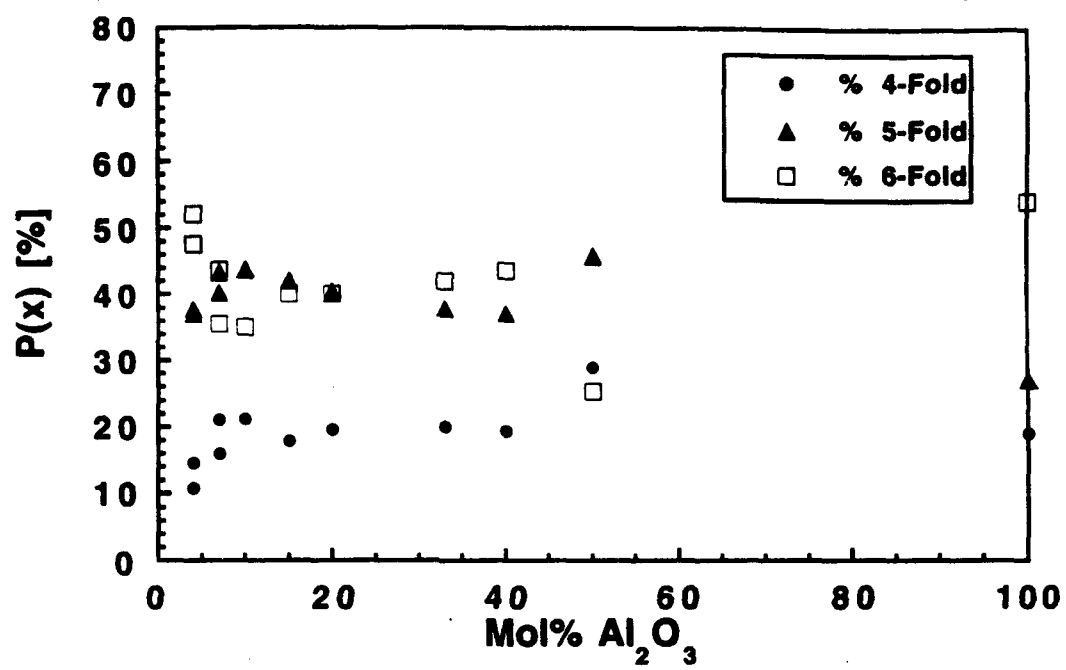


Figure 5

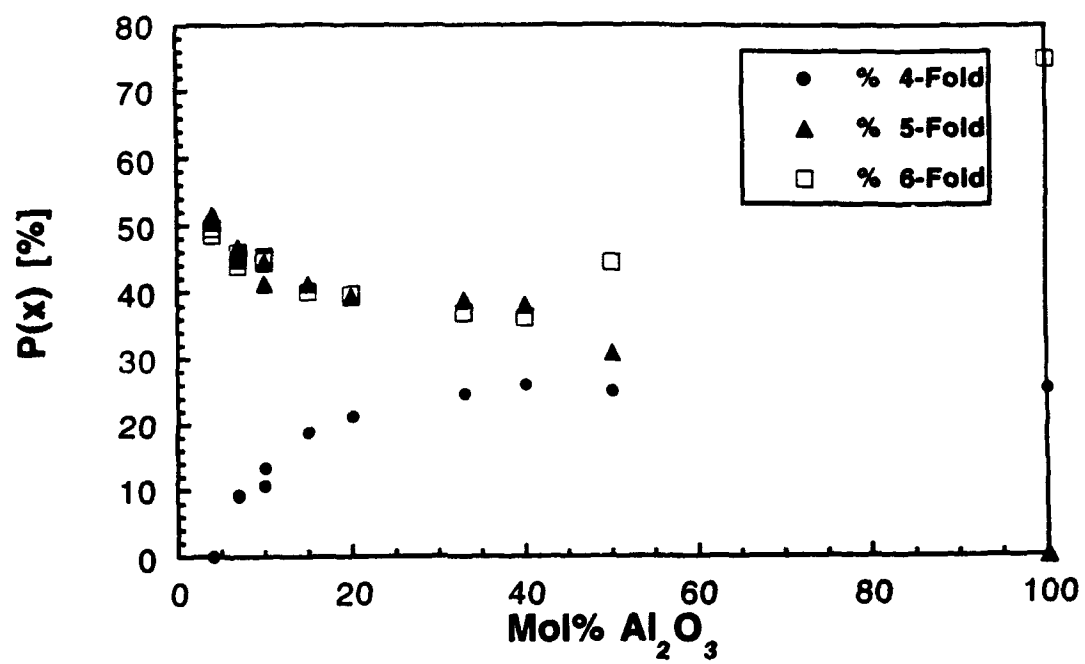


Figure 6



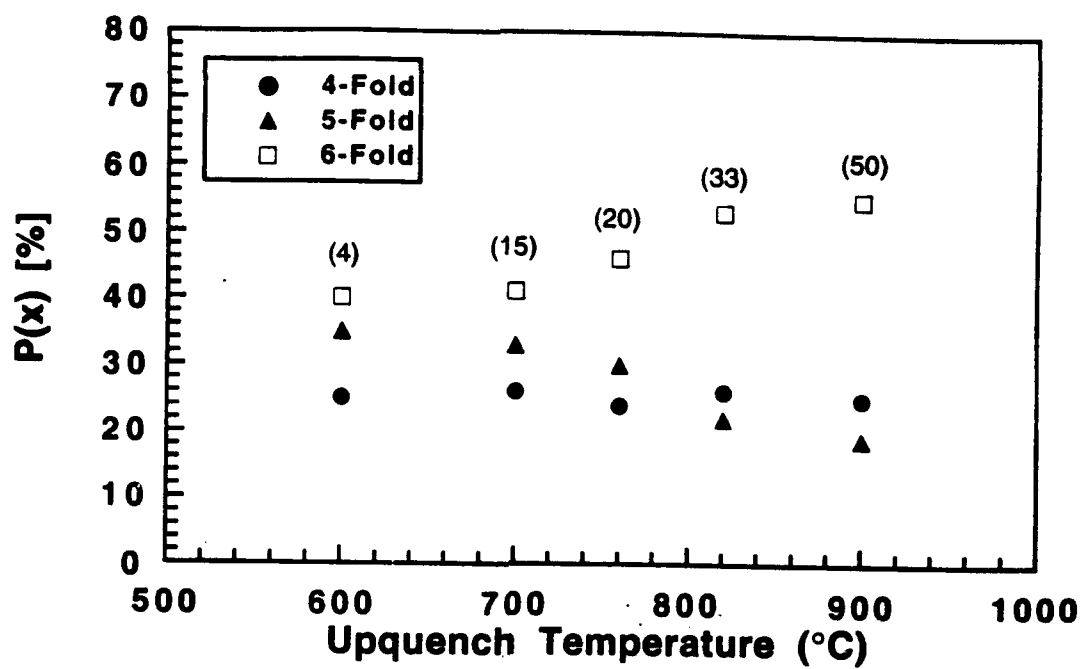


Figure 7

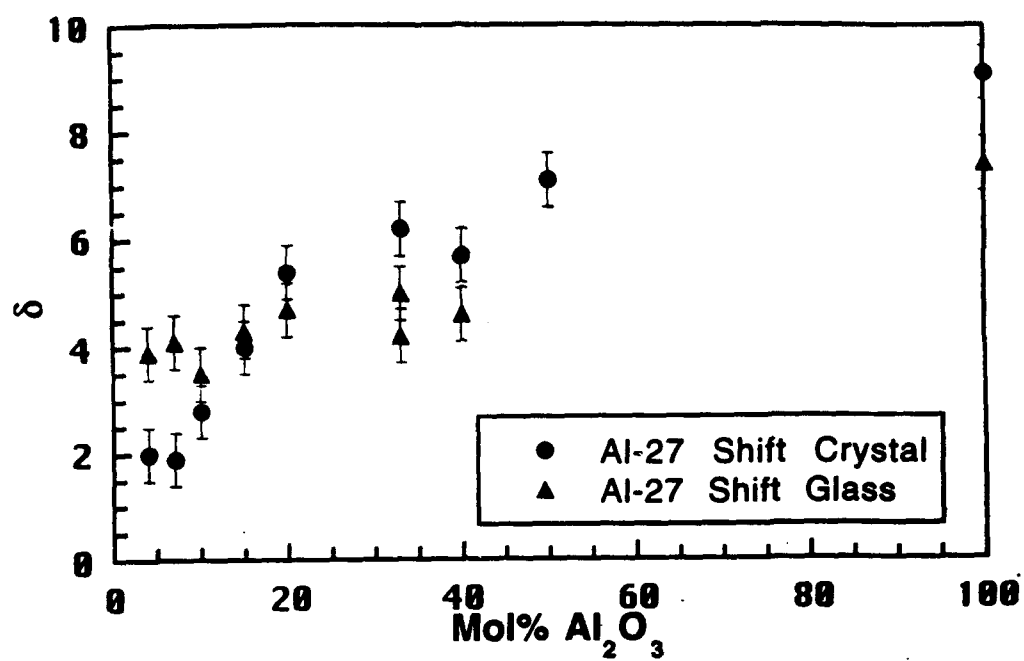


Figure 8

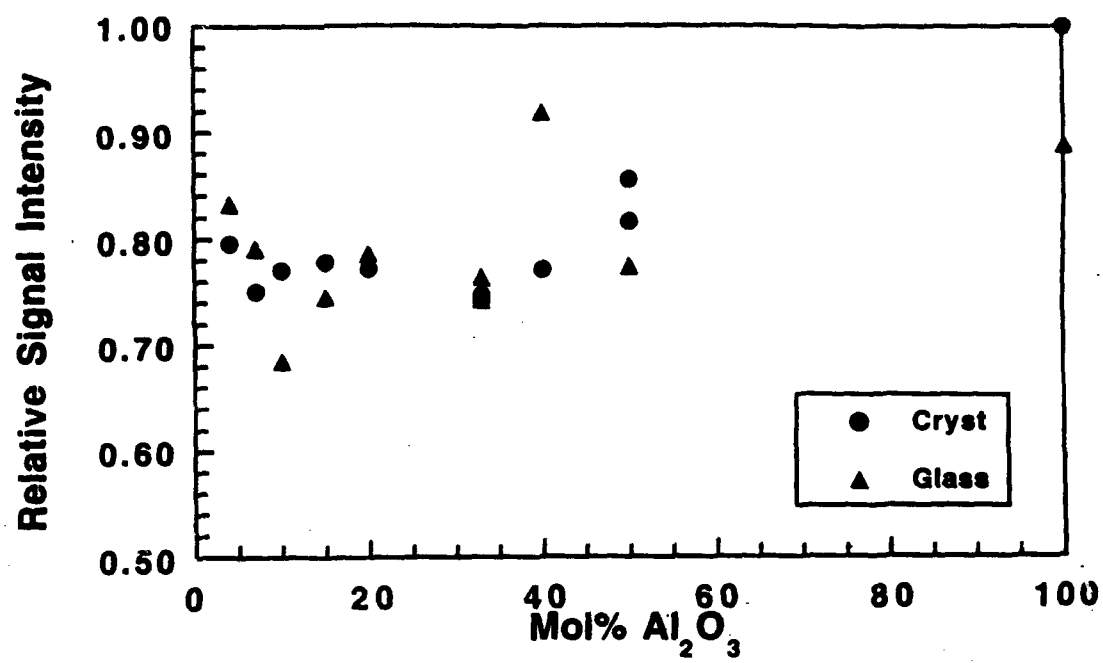


Figure 9

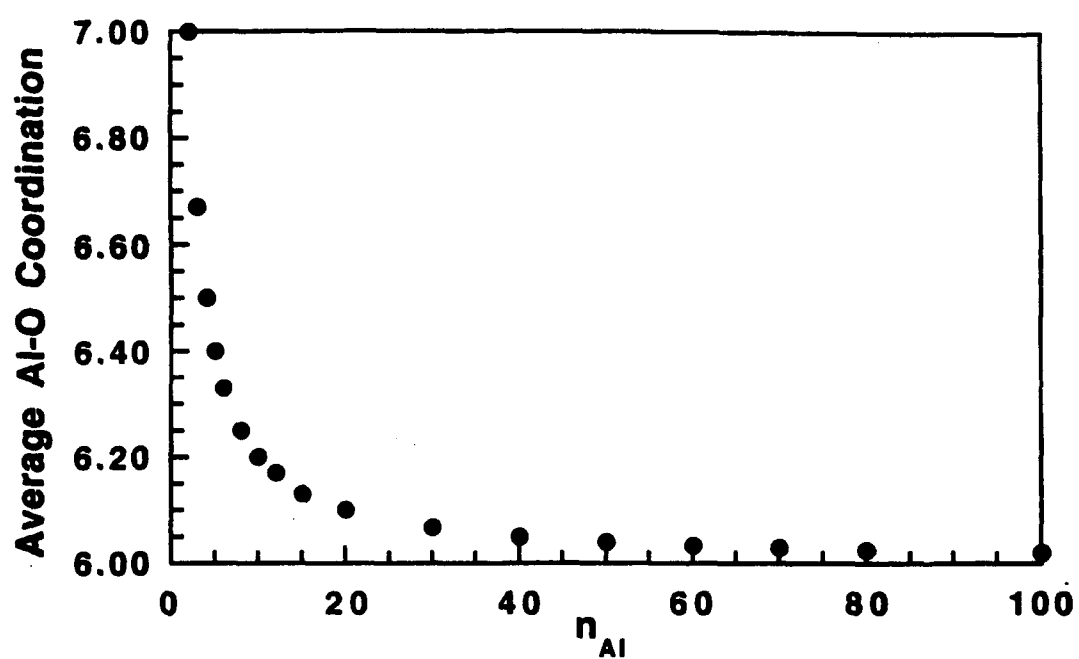


Figure 10

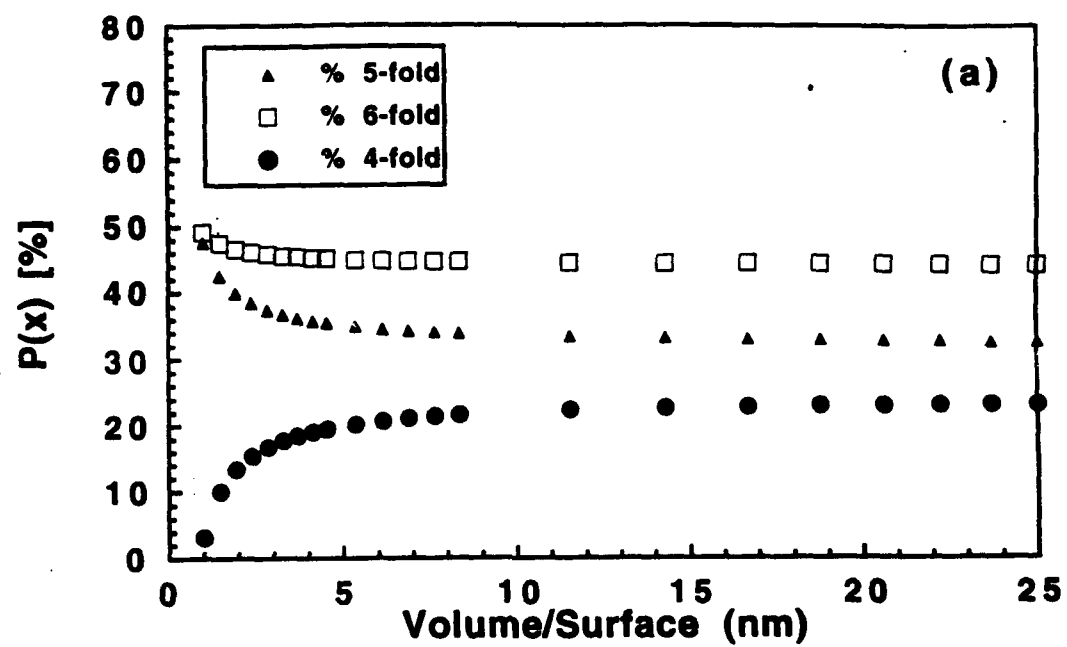


Figure 11

**High Temperature Stability of Binary Microstructures  
Derived From Liquid Precursors**

**Contract AFOSR-91-0125**

**Technical Report No. 12**

**Epitaxial Growth of  $\text{PbTiO}_3$  Thin Films on  
 $\{100\}$   $\text{SrTiO}_3$  from Solution Precursors**

**Andreas Seifert, Fred F. Lange and James S. Speck**

**Materials Department  
College of Engineering  
University of California  
Santa Barbara, CA 93106**

**Final Report, June 30, 1994**

**Principal Investigator: Fred F. Lange 805 893 8248**

**Sent to Journal of the Materials Research Society**

**Epitaxial Growth of PbTiO<sub>3</sub> Thin  
Films  
on (001) SrTiO<sub>3</sub>  
from Solution Precursors**

**Andreas Seifert, Fred F. Lange and James S. Speck**

**Materials Department  
College of Engineering  
University of California  
Santa Barbara, California 93106**

## Abstract

A mixed alkoxide liquid precursor was used to form epitaxial  $\text{PbTiO}_3$  thin films by spin-coating on cubic (001)  $\text{SrTiO}_3$  substrates. The films were heat-treated at temperatures between  $380^\circ\text{C}/1\text{h}$  and  $800^\circ\text{C}/1\text{h}$ . X-ray diffraction, atomic force microscopy, scanning and transmission electron microscopy were used to characterize the microstructure of the films and to evaluate the epitaxial phenomena. At  $\sim 400^\circ\text{C}/1\text{h}$ , a polycrystalline, metastable Pb-Ti-fluorite crystallizes from the pyrolyzed amorphous precursor. At slightly higher temperatures ( $\sim 420^\circ\text{C}/1\text{h}$ ), the thermodynamically stable phase with the perovskite structure epitaxially nucleates at the film/substrate interface. A small number of epitaxial grains grow through the film toward the surface and consume the nano-crystalline fluorite grains. Coarsening of the perovskite grains leads to a reduction in mosaic spread during further heating. Pores, that concurrently coarsen with grain growth, produce a pitted surface as they disappear from within the film. At  $800^\circ\text{C}/1\text{h}$  a dense epitaxial  $\text{PbTiO}_3$  film with a smooth surface is observed. Parameters governing the formation of *a*- and *c*-domains are discussed as well as the small tilts of the domain axes away from the substrate normal.



## 1. Introduction

Single crystal ferroelectric thin films are preferred to polycrystalline films for a range of optical and electronic applications.<sup>1</sup> Kingon<sup>2</sup>, for example, has shown that the single crystal films have improved aging and fatigue behavior in non-volatile memory applications. The pyroelectric properties of  $\text{PbTiO}_3$  are optimal along the polar direction, thus single crystal films are preferred for pyroelectric devices.<sup>3</sup> Also, devices that use optical transmission require films that do not scatter light. A number of techniques have been employed to grow either oriented or epitaxial thin films of ferroelectric lead titanate, lead titanate zirconate (PZT) and lanthanum modified PZT (PLZT) on single crystal substrates including  $\text{MgO}$ ,<sup>3-5,13</sup>  $\text{SrTiO}_3$ ,<sup>6,12</sup>  $\text{MgAl}_2\text{O}_4/\text{Si}$ ,<sup>11</sup>  $\text{YBa}_2\text{Cu}_3\text{O}_7/\text{LaAlO}_3$ ,<sup>9</sup>  $(\text{La,Sr})\text{CoO}_3/\text{SrTiO}_3$ ,<sup>8</sup>  $(\text{La,Sr})\text{CoO}_3/\text{MgO}$ ,<sup>8</sup>  $(\text{La,Sr})\text{CoO}_3/\text{Zr}(\text{Y})\text{O}_2/\text{Si}$ ,<sup>10</sup>  $\text{Pt}/\text{MgO}$ ,<sup>3,5</sup> as well as  $\text{Pt}/\text{Ti}/\text{SiO}_2/\text{Si}$ .<sup>5,7</sup> Deposition methods include radio frequency sputtering,<sup>3-7</sup> pulsed laser deposition,<sup>8-10</sup> and chemical vapor deposition.<sup>11-13</sup>

A small number of groups have been processing thin films by solution chemistry routes. In these methods, a precursor solution<sup>14,15</sup> containing metal-organic molecules in either an aqueous or organic solvent is used to form a solid precursor film on a substrate by either spin-coating<sup>16</sup> or dip-coating.<sup>17</sup> During coating the solvent evaporates to produce a solid, amorphous precursor film. The precursor film decomposes (pyrolyzes) and crystallizes during heating at low temperature to form a partially dense, polycrystalline thin film of the desired inorganic composition.

The mechanisms leading to epitaxy in precursor derived films are different from phenomena associated with vapor phase epitaxy.<sup>18</sup> Several of these mechanisms have been identified.<sup>19</sup> Miller et al.<sup>20</sup> have shown that when the film and substrate have the same crystal structure, and the lattice mismatch is small, oriented nano-crystallites in contact with the substrate eventually grow along the

film/substrate interface and then through the film to consume all randomly oriented grains. This process was called epitaxial grain growth. The same mechanism is likely for heteroepitaxy of tetragonal  $\text{Zr(Y)O}_2$  compositions on (001) cubic zirconia substrates.<sup>21</sup> Even when the film and substrate have unrelated structures, epitaxial films are possible but they are formed by an intermediate step that causes the polycrystalline film to break into isolated epitaxial grains.<sup>22</sup> These isolated grains can then be used as seeds to form a continuous film after the substrate is recoated and reheated. Vaidya et al.<sup>23</sup> have shown that the oxide precursor may react with the substrate and form an epitaxial thin film. Epitaxial films may also form at higher temperatures through a liquid phase process.<sup>24</sup>

A variety of different precursor chemistries and substrates have been used to produce single crystal ferroelectric films. Sapphire substrates were used for Nb-doped PZT thin films.<sup>25</sup> The growth of highly oriented PZT 53/47 ( $\text{PbZr}_{0.53}\text{Ti}_{0.47}\text{O}_3$ ) films was reported by Schwarz et al.<sup>26</sup> on (001)  $\text{SrTiO}_3$ . Hirano et al.<sup>27</sup> studied the influence of a wet oxygen atmosphere on the pyrolysis and orientation of PZT 53/47 films formed on (001)  $\text{SrTiO}_3$ , (001)  $\text{MgO}$  and platinized silicon. Tuttle et al.<sup>28</sup> grew highly textured PZT 40/60 on (001)  $\text{Pt/MgO}$  and on (001)  $\text{MgO}$ . Epitaxial PLZT films on  $\text{SrTiO}_3$  were reported by Yoon et al.<sup>29</sup>

The goal of the current study was to identify the epitaxy mechanism for the  $\text{PbTiO}_3$  (PTO) film formation on (001)  $\text{SrTiO}_3$  (STO) single crystal substrates. STO was chosen as the substrate because its lattice parameters at the growth temperature of  $\text{PbTiO}_3$  (above the Curie temperature,  $T_c = 490^\circ\text{C}$ ) are similar to the parameters of cubic paraelectric (PE) PTO. At  $800^\circ\text{C}/1\text{h}$  for example,  $a_{\text{PTO}}$  is 0.3975 nm and  $a_{\text{STO}}$  equals 0.3938 nm. Thus the unrelaxed, linear in-plane strain is about 1%, and much smaller than for other oxide substrates such as  $\text{MgO}$  or  $\text{MgAl}_2\text{O}_4$ . Also, the thermal expansion mismatch between STO and PTO above  $T_c$  is relatively small ( $\alpha_{\text{PTO}} = 12.6 \times 10^{-6}/\text{K}$  ( $T > 490^\circ\text{C}$ ) and  $\alpha_{\text{STO}} = \sim 11 \times 10^{-6}/\text{K}$  ( $20^\circ\text{C} - 1000^\circ\text{C}$ )). During cooling

through  $T_c$ ,  $\text{PbTiO}_3$  transforms to a tetragonal ferroelectric and below  $T_c$  the tetragonal a-axis of PTO ( $a_{\text{PTO}} = 0.3904 \text{ nm}$ ,  $c_{\text{PTO}} = 0.4152 \text{ nm}$ , at room temperature) becomes closely matched to the cubic STO lattice parameter ( $a_{\text{STO}} = 0.3905 \text{ nm}$ ).

Most studies of  $\text{PbTiO}_3$ , PZT or PLZT perovskite films report a metastable intermediate phase at lower processing temperatures. This phase is usually described as 'pyrochlore'.<sup>3,5,30-35,44</sup> The pyrochlore phase is generally seen as a disadvantage because it can be retained after processing at high temperatures and it is known to deteriorate the ferroelectric properties of the films.<sup>34</sup> In our study we have found that the crystallization of the Pb-Ti-fluorite may be *advandageous* for low temperature epitaxy of  $\text{PbTiO}_3$ . Formation of the intermediate fluorite reduces the free energy in the  $\text{PbO-TiO}_2$  system and thus *promotes* selective heterogeneous nucleation of epitaxial perovskite at the film/substrate interface. However, because the fluorite-to-perovskite transformation takes place rapidly at low temperature, unwanted porosity, present in the low density fluorite film, becomes entrapped within the epitaxial film. This aspect of the fluorite to perovskite transformation is a disadvantage since higher processing temperatures of  $\sim 0.69 \cdot T_{\text{melting}}$  of  $\text{PbTiO}_3$  are needed to eliminate the entrapped porosity and to form a smooth and epitaxial film.

## 2. Experimental

Lead Titanate thin films were prepared by spin coating (Headway Research Inc., Garland, TX)  $\text{SrTiO}_3$  (Coating & Crystal Technology Inc., Kittanning, PA) substrates with a double alkoxide precursor synthesized by the method introduced by Gurkovich and Blum.<sup>36</sup> In this synthesis, previously assayed lead acetate hydrate,  $\text{Pb}(\text{CH}_3\text{COO})_2 \cdot 3.3\text{H}_2\text{O}$ , was placed in a 3-neck flask, fitted with a reflux condenser, and dissolved at  $70^\circ \text{C}$  in 2-methoxy ethanol ( $T_b = 124^\circ \text{C}$ ),  $\text{C}_3\text{H}_8\text{O}_2$ .

Water was removed from lead acetate hydrate by distillation at  $\sim 120^{\circ}\text{C}$  for 1h. After cooling to  $70^{\circ}\text{C}$ , titanium-isopropoxide,  $\text{Ti}(\text{OC}_3\text{H}_7)_4$  was stirred into the solution under nitrogen to produce a composition with a 1:1 Pb:Ti ratio. The solution was then boiled and refluxed for one hour to allow the formation of the Pb-Ti double-alkoxide. A Fourier Transform Nuclear Magnetic Resonance study by Ramamurty and Payne<sup>37</sup> has shown that short-chain oligomers, with -Ti-O-Pb- bonds, form during refluxing. The precursor viscosity was adjusted by distilling some of the solvent and the double-alkoxide was stored under nitrogen. No additions were made to stabilize or pre-hydrolyze the precursor. For an assay, 5 ml of the precursor was poured into an alumina crucible and allowed to react with atmospheric moisture. After drying overnight, the gel was heated ( $5^{\circ}\text{C}/\text{min.}$ ) to  $600^{\circ}\text{C}$  for one hour. Gravimetric analysis showed the solution contained 0.55 mols of  $\text{PbTiO}_3$ . The assayed powder was examined by X-ray diffraction (XDS2000, Scintag Inc., Sunnyvale, CA) using silicon as an internal standard.

Polished, cubic single crystal, (001) oriented  $\text{SrTiO}_3$  substrates were used in this study. The substrates were cleaned by rinsing in tri-chloro-ethane, acetone and iso-propanol to remove organic contamination. Ultrasonic cleaning was avoided because it was found to cause surface damage, as determined by optical microscopy. After cleaning, the substrates were heated to  $1400^{\circ}\text{C}$  for 2h to remove polishing damage. The annealed substrates were stored in a vacuum-dessicator. Just prior to spin-coating, the double-alkoxide precursor was transferred, under nitrogen, to a pipette. The pipette was fixed in a device above the spin-coater and flushed continuously with nitrogen to prevent premature hydrolysis. After deposition by spin-coating (5000 rpm for 30 s), the films were kept in air for at least 0.5 h to allow the thin alkoxide precursor films to react with atmospheric water, before any heat treatment.

As reported below, lead loss during heat-treatment was found to hinder epitaxy. To minimize lead loss, the specimens were placed in a covered, subdivided alumina boat containing PbO powder. Heat-treatments (5°C/min) at temperatures between 350°C and 800°C were carried out in a tube furnace under flowing (~12 cm<sup>3</sup>/min) instrument grade oxygen followed by cooling to room temperature at 10°C/min. Specimens heated to temperatures  $\geq 450^\circ\text{C}$  were held for one hour at 450°C to ensure complete pyrolysis<sup>30,38</sup> before heating to higher temperatures.

To evaluate the process of crystallization, epitaxy, and microstructural evolution, thin films heat-treated at different temperatures were examined by X-ray diffraction (XDS2000, Scintag Inc., Sunnyvale, CA, and MRD, Philips, Eindhoven, The Netherlands), Atomic Force Microscopy (AFM; Nanoscope III, Digital Instruments Inc., Santa Barbara, Ca), Scanning Electron Microscopy (SEM; JEOL 6300FE, Tokyo, Japan) and Transmission Electron Microscopy (TEM; JEOL 2000FX, 4000FX, 4000EX).

### 3. Results

#### 3.1 Effect of PbO Environment on Microstructural Development

Heat-treatments of the thin films were initially performed *without* PbO powder adjacent to the specimens. Lead-loss at heat-treatment temperatures of 500°C - 650°C was found to hinder grain coarsening and the epitaxial phenomena as detailed below. Unidentified Pb-deficient second phases formed at temperatures between 700°C and 800°C and were observed in TEM specimens by energy dispersive spectroscopy. To control lead-loss, all further heat-treatments were carried out with the specimens placed adjacent to PbO powder in a subdivided, covered alumina boat.

### 3.2 X-ray Diffraction of Powder

A  $\Theta$ - $\Theta$  X-ray diffraction scan of  $\text{PbTiO}_3$  powder synthesized from the double-alkoxide precursor and heated to  $600^\circ\text{C}/1\text{h}$  showed phase-pure tetragonal  $\text{PbTiO}_3$  perovskite with lattice parameters of  $a_{\text{PTO}} = 0.3907 \text{ nm}$  and  $c_{\text{PTO}} = 0.413 \text{ nm}$  determined with a silicon internal standard. The reason for the small differences between these and literature values<sup>39</sup> ( $a_{\text{PTO}} = 0.3904 \text{ nm}$  and  $c_{\text{PTO}} = 0.4152 \text{ nm}$ ) is unknown.

### 3.3 X-ray Diffraction of Films Heat-Treated in a $\text{PbO}$ Environment

$\Theta$ - $\Theta$  X-ray diffraction scans of the  $\text{PbTiO}_3$  thin films were performed after maximizing the intensity of the  $\{002\}$  STO substrate reflection (achieved by maximizing intensities in  $\Theta$ - $\Theta$ ,  $\omega$ - (rocking) and  $\chi$ - (azimuth) scans). For the films heated at temperatures of  $450^\circ\text{C}$  and above, only the  $(00l)$  tetragonal  $\text{PbTiO}_3$  reflections were observed;  $(h00)$  diffraction peaks were masked by the strong substrate peak. No other reflections for either  $\text{PbTiO}_3$  or any other phase were detected. As shown in Fig. 1, the intensity of the  $(002)$  reflections strongly increased with increasing heat-treatment temperatures between  $450^\circ\text{C}/1\text{h}$  to  $800^\circ\text{C}/1\text{h}$ , consistent with an oriented PTO film (all scans in Fig. 1 were normalized such that the  $\{003\}$   $\text{SrTiO}_3$  substrate reflections were approximately the same intensity for all heat-treatments). The intensities of  $(002)$   $\text{PbTiO}_3$  reflections of films heated at  $675^\circ\text{C}/1\text{h}$  and  $800^\circ\text{C}/1\text{h}$  were nearly identical, indicating that the apparent orientational quality of the films were similar between these temperatures. Because of the low scattering strength of thin polycrystalline films, X-ray diffraction results from randomly oriented films had to be carefully scrutinized. For example, we were unable to detect any film reflections for specimens heated at temperatures

between 380°C/1h and 420°C/1h, although the presence of a distinct randomly oriented crystalline phase was observed for the same specimens by TEM.

To determine the exact orientation of the ferroelectric domains (twins) in the epitaxial film heated at 800°C/1h, high resolution X-ray diffraction pole figure scans (Philips, MRD) were recorded for the  $\text{PbTiO}_3$  (002) and (200) reflections. These scans were limited to a small portion of the hemispherical diffraction space about the surface normal. Figure 2a shows an intensity-contour plot of the limited pole figure for the  $\text{PbTiO}_3$  (002) reflection. It shows four specific orientations for the (001) planes of the *c*-domains ( $c_{\text{PTO}} \perp$  film/substrate interface) in the film, and shows that the *c*-domains are rotated about  $\langle 100 \rangle_{\text{STO}}$  and  $\langle 010 \rangle_{\text{STO}}$ , away from the substrate normal  $[001]_{\text{STO}}$ , by approximately 0.7°. The rocking-curve for PTO (002) at  $\psi = -0.3^\circ$ , as shown in Fig. 2b, can be fit to two over-lapping Gaussians. The full width half maximum (FWHM) of the individual Gaussians is  $\sim 0.9^\circ$  and  $\sim 0.8^\circ$ , respectively. A pole figure scan for PTO (200) is shown in Fig. 2c. It also shows four different orientations for the (*h*00) planes of the *a*-domains ( $c_{\text{PTO}} \parallel$  film/substrate interface). The *a*-domain rotation-angle of  $\sim 2.2^\circ$  about  $\langle 100 \rangle_{\text{STO}}$  and  $\langle 010 \rangle_{\text{STO}}$ , away from the substrate normal  $[001]_{\text{STO}}$ , is larger than for the *c*-domains. The rocking curve of one of the *a*-domain orientations at  $\psi = -0.3^\circ$  and  $\Delta \omega = 2.2^\circ$  shows a similar FWHM of  $\sim 0.7^\circ$  (Fig. 2d) as determined for the *c*-domains.

### 3.4 SEM of Films Heat-Treated in a PbO Environment

Specimens of films heat-treated between 450°C/1h and 800°C/1h were examined with a field-emission SEM using a 5 kV accelerating voltage. The microstructural development of these films is shown in Fig. 3. At 450°C/1h the film consists of nanometer grains and pores (Fig. 3a). At lower temperatures of 380°C/1h or 420°C/1h, fine scale microstructural features were unresolvable by SEM. Figure 3b shows that after heat-treating at 625°C/1h both pores and grains

have undergone significant coarsening ( $\approx 100$  nm). Despite its polycrystalline appearance, the  $\Theta-\Theta$  scans shown in Fig. 1 indicate a {001} textured film. At 675°C/1h, Fig. 3c shows residual grains on top of a strongly pitted and faceted film, indicating almost complete epitaxy - this is consistent with the X-ray diffraction pattern shown in Fig. 1. At 800°C/1h, the film is free of facets and residual grains on the surface as shown in Fig. 3d. Large terraces of several microns in size and smaller scale rectangular features corresponding to ferroelectric *c*- and *a*-domains (0.1 and 0.3  $\mu\text{m}$ ) can be observed. Imaging of ferroelectric domains in the SEM is facilitated by using an accelerating voltage close to the cross-over voltage of the film<sup>40</sup> ( $\sim 5$  kV for  $\text{PbTiO}_3$ ). Voltage contrast is caused by the differently polarized ferroelectric *a*- and *c*-domains. This observation is consistent with TEM and AFM results.

### 3.5 TEM of Films Heat-Treated in a PbO Environment

Figure 4a illustrates that a film heated for one hour at 380°C contains randomly oriented, nanometer grains embedded in an apparently amorphous matrix, as determined with TEM tilting experiments and selected area diffraction (no experiments were performed to determine the length scale of order in the amorphous matrix). Crystallization continues throughout the film until at 400°C/1h the entire layer consists of the randomly oriented grains. SAD of the film heated at 400°C/1h in Fig. 4b shows that the grains have a fluorite structure with a lattice-parameter of  $a \approx 0.49$  nm. No superlattice reflections, typical for the related pyrochlore structure ( $\text{Pb}_2\text{Ti}_2\text{O}_6$   $a \approx 1$  nm), could be observed. High resolution TEM (HRTEM) could not establish any particular orientation relationship between the fluorite grains and the substrate.

Continued heating to 420°C/1h initiates a phase transformation from the Pb-Ti-fluorite to tetragonal  $\text{PbTiO}_3$  perovskite at the film/substrate interface. The



perovskite then grows to consume all of the fluorite phase (Fig. 5). SAD of film and substrate (inset in Fig. 5a) and dark field (DF) imaging with the (020)-substrate/film reflection (Fig. 5b) showed that the perovskite grains were highly {001}<sup>a)</sup> aligned. At 450°C/1h the film has completely transformed to an oriented, porous, tetragonal perovskite with a mosaic spread of ~ 10°.

When heated to 650°C/1h, the mosaic spread was reduced significantly as shown in the inset SAD pattern in Fig. 6a. Residual porosity and ferroelectric domains are shown in Figs. 6a and 6b by bright and dark field TEM, respectively. Dark field imaging with the (002) reflection, containing diffraction information of both film and substrate, suggests that the formation of the epitaxial layer is complete. After heat-treatment at 675°C/1h (Fig. 7), the residual porosity and mosaic spread are greatly reduced, but facets and large residual grains are present on the surface of the film, as shown earlier with SEM (Fig. 3). Surface smoothing by either evaporation-condensation or surface diffusion was achieved for a PbTiO<sub>3</sub> film heated at 800°C/1h. Figure 8 illustrates the ferroelectric domain structure and the low threading dislocation density of the films heated at 800°C/1h. No threading dislocations were found over all of the electron transparent area of the cross-section sample. Assuming a volume of 0.1 x 0.1 x 50 μm, the threading dislocation density must have an upper limit of ~ 2 x 10<sup>7</sup> cm<sup>-2</sup>.

Figure 9 illustrates (via HRTEM) that the narrow twins are *a*-domains (*c*-axis || film/substrate interface) and the wide twins are *c*-domains (*c*-axis ⊥ film/substrate interface). Strain contrast resulting from misfit dislocations at the interface of *c*-domains with the substrate can be seen in Fig. 8. A similar contrast can be observed at the intersection of domain boundaries with the substrate. In the latter case, the

---

<sup>a)</sup> For simplicity we call the film '{001} oriented'. The actual epitaxial relationship is as follows: (001)[100]<sub>PbTiO<sub>3</sub></sub> || (001)[100]<sub>SrTiO<sub>3</sub></sub>.

contrast stems from interfacial disclinations resulting from the equilibrium tilts in *a*- and *c*-domains due to twinning.<sup>41</sup> The relative tilt of approximately 3.5° between *a*- and *c*-domains was measured from the orientation of lattice fringes in Fig. 9. Also, the change of the surface orientation of the *a*-domains as a result of twinning is illustrated in Fig. 9. The morphology associated with surface orientation may be used to image the ferroelectric domains with the Atomic Force Microscope as shown in Fig. 10. The tilts in *a*- and *c*-domains could be detected by SAD parallel to [100], as described elsewhere.<sup>41</sup> For *a*-domains it was found that the relative rotation of [010]<sub>PTO</sub> (⊥ to the film/substrate interface) about <100><sub>STO</sub> and <010><sub>STO</sub> is approximately 3° from the substrate normal [001]<sub>STO</sub>. For [001]<sub>PTO</sub> (⊥ to the film/substrate interface) of the *c*-domains a rotation of only ~ 0.5° from the substrate normal [001]<sub>STO</sub> about <100><sub>STO</sub> and <010><sub>STO</sub> could be detected. These results are in agreement with X-ray pole figure results shown in Fig. 2.

#### 4. Discussion

Cross-sectional TEM characterization showed how a precursor solution processed thin film develops into an epitaxial tetragonal perovskite PbTiO<sub>3</sub> thin film. The sequential steps in this process include: i) the initial crystallization of the amorphous film to a partially dense, nano-crystalline fluorite phase with a smooth surface morphology; ii) the transformation of the fluorite film to a porous, highly {001} textured perovskite film; iii) reduction of the mosaic spread and porosity to produce a single crystal PbTiO<sub>3</sub> thin film with a pitted surface morphology; and iv) the elimination of surface pits at 800°C to produce a smooth and epitaxial PTO thin film.

When the thin films were heat-treated in a furnace *without* adjacent PbO powder, SEM and X-ray diffraction studies showed that the microstructural

evolution arrested at a stage where the film had a large mosaic spread and contained large pores. Further heat-treatment lead to the formation of uncharacterized second phases with a lower Pb/Ti ratio relative to  $\text{PbTiO}_3$ .

#### 4.1 Crystallization of the Fluorite Phase

Our study clearly demonstrated that the crystallization of the stoichiometric  $\text{PbTiO}_3$  precursor to the perovskite structure occurs through an intermediate fluorite phase. This appears to confirm the observation of an 'unknown intermediate phase' in an early powder X-ray study by Blum and Gurkovich.<sup>30</sup> Other researchers<sup>3,5</sup> have also reported that sputtered  $\text{PbTiO}_3$  films crystallize with a fluorite structure at low deposition temperatures.

Because precursors pyrolyze to an inorganic material at low temperatures relative to the melting temperature, the free energy change for crystallization,  $\Delta G_c$ , is large, and the critical nucleus size required for spontaneous crystallization is small. Thus, the crystallization of a connective (partially sintered) network of nano-crystallites is commonly observed; crystallization typically occurs at temperatures where long-range diffusion is kinetically limited and thus metastable phases often crystallize.<sup>42,43</sup> In the present case, the crystallization of the fluorite phase instead of the thermodynamically stable perovskite is another example of kinetically limited crystallization. Transformation and/or decomposition to more stable structures requires heating to temperatures where long range diffusion becomes kinetically viable.

Metastable crystallization of precursors to fluorite or pyrochlore during synthesis of  $\text{Pb}(\text{Zr},\text{Ti})\text{O}_3$  compositions is commonly observed.<sup>44</sup> In the current case, a Pb-Ti-fluorite phase with  $a = 0.49$  nm crystallized instead of the structurally related pyrochlore phase. The absence of any superlattice reflections (that would appear for the ordered pyrochlore structure with  $a = 1.05$  nm) confirms an observation by

Wilkinson et al.,<sup>31</sup> stating that although the intermediate phase is often called "pyrochlore", superlattice reflections that would indicate the higher degree of order in the pyrochlore were actually rarely reported.  $A_2B_2O_{7-x}$  pyrochlores in general can be seen as "2 x 2 x 2" (8 unit cells) fluorites with 8-coordinated A- and 6-coordinated B-cations.<sup>45</sup> Ordering of the oxygen vacancies in the structure cause the doubling of the cell length compared to a regular fluorite. Cation and oxygen vacancy ordering has been observed in the crystallization of non-stoichiometric fluorites when exposed to higher heat-treatment temperatures. For example, Jayaram et al.<sup>46</sup> have shown that  $(Y,Zr)_2O_3$  solid-solutions first crystallize with the fluorite structure because of the random distribution of the oxygen vacancies and then transform to the preferred cubic-rare earth oxide structure at higher temperatures where sufficient diffusion allows vacancy ordering. Similarly, because in the fluorite structure, neither  $Pb^{2+}$  and  $Ti^{4+}$  nor the oxygen vacancies need to order during diffusion limited crystallization, it might be expected that the fluorite would be selected as the metastable phase prior to  $PbTiO_3$  perovskite crystallization. The transformation from either the fluorite or pyrochlore to the perovskite structure at higher heat-treatment temperatures requires a reconstruction of the oxygen sites from a simple cubic to a face centered cubic arrangement. In the kinetically limited crystallization of  $PbTiO_3$ , the fluorite can thus be considered a more compositionally flexible phase than the perovskite. In this regard it is interesting to note that PZT perovskite, for example, has been reported to accommodate only 2 mol% PbO-deficiency<sup>47</sup> in equilibrium at 1000°C.

Using the schematic free energy diagram in Fig. 11 to understand diffusion limited crystallization, it can be seen that during crystallization of a *stoichiometric* Pb-Ti-precursor (path 1), the free energy change  $\Delta G_c$  is large for the formation of the kinetically favored intermediate fluorite phase. The system further lowers its free energy by  $\Delta G_{f-p}$  during the reconstructive phase transformation to the

thermodynamically stable perovskite. Because of its ability to accommodate disordered oxygen vacancies, the fluorite structure might also be considered to be the more stable structure for the partitionless crystallization of non-stoichiometric compositions (path 2, Fig. 11), as represented by the broader free energy curve of the fluorite phase relative to the perovskite phase shown in Fig. 11. Heat-treatments at higher temperatures allow diffusion and will lead to partitioning of the metastable fluorite into two phases (e.g., PbO + Perovskite-PbTiO<sub>3</sub>), driven by a further decrease of the free energy  $\Delta G_p$ .

The most important cause for non-stoichiometry in the PbO-TiO<sub>2</sub> and PbO-TiO<sub>2</sub>-ZrO<sub>2</sub> systems appears to be the loss of lead due to its volatility during heating. Gradual lead-loss causes local non-stoichiometry on the lead-poor side of the PbO-TiO<sub>2</sub> phase diagram and may promote fluorite formation as suggested in Fig. 11. To compensate lead-loss, it has become common practice to use precursors with 5-10 mol% of excess lead<sup>28,34,35</sup> or, in the case of sputtering, to use targets containing up to 30% excess Pb (or PbO).<sup>3</sup> Because lead-loss takes place gradually, lead-rich non-stoichiometric compositions will promote fluorite formation in the early stages of the heat-treatment as suggested in Fig. 11. Therefore it seems advantageous to employ other methods to control the lead-content of the films. Tani et al.<sup>44</sup>, for example, have used a PbO-overcoat on top of PLZT films. In our study, we have successfully employed a Pb-rich atmosphere from PbO during heat-treatment of the stoichiometric precursor films. The PbO vapor pressure over PbO is approximately two orders of magnitude higher than over PbTiO<sub>3</sub>,<sup>47</sup> and thus prevents lead-loss from the film into the atmosphere.

It also is likely that an increase of the number of species in the system (e.g. PZT compared with PbTiO<sub>3</sub>) increases the possibility for global and local non-stoichiometry and thus for fluorite formation. The stronger tendency of Pb(Ti,Zr)O<sub>3</sub> compositions containing Zr to form and retain the fluorite phase has

been widely reported in the literature.<sup>3,28,30-35,38,44</sup> In an *in-situ* X-ray diffraction study, Wilkenson et al.<sup>31</sup> have observed fluorite formation for PZT and PbZrO<sub>3</sub> compositions but not for PbTiO<sub>3</sub>. However, the chosen time and temperature interval may have missed a fleeting fluorite phase before its transformation to PbTiO<sub>3</sub> perovskite. It has been noted that the tendency of Zr<sup>4+</sup> to be coordinated by more than six oxygens, is more likely to be accommodated by the defect-fluorite structure than the rigid perovskite structure with only 6-coordinated B-cations.<sup>31</sup> Yamaguchi et al.,<sup>48</sup> for example, discuss PbZrO<sub>3</sub> as the end member of a fluorite solid-solution series in the PbO - ZrO<sub>2</sub> binary system.

For polycrystalline, as well as epitaxial PZT films, it has been shown that rapid thermal annealing at rates on the order of 100°C/s can minimize or even avoid fluorite formation.<sup>28,49</sup> It appears that the high heating rate might minimize the density of fluorite nuclei and promote the direct crystallization of the perovskite by moving rapidly to the temperature where long range diffusion is concurrent with crystallization.

#### 4.2 Role of the Fluorite → Perovskite Transformation in the Epitaxy Phenomenon

The observed epitaxy phenomenon of PbTiO<sub>3</sub> on SrTiO<sub>3</sub> is very different than that studied by Miller et al.<sup>20</sup> for solution derived cubic-ZrO<sub>2</sub> on cubic-ZrO<sub>2</sub> substrates. Although the initial crystallization was similar to that observed here, namely, the film directly crystallized into partially dense nano-crystalline ZrO<sub>2</sub>, two phenomena were very different. First, the ZrO<sub>2</sub> nano-crystallites formed during crystallization had the same structure as the underlying substrate. Second, the nano-crystallites touching the substrate had the same crystallographic orientation as the substrate. It was these oriented crystallites that first grew across the film/substrate interface and then grew up to the film surface to produce a uniform conversion to a single crystal film. The driving force for this conversion was the

free energy change associated with elimination of grain boundary energy per unit volume.

In the current study, the initial polycrystalline film did not have the same structure as the substrate, and the driving force for the nucleation and growth of the epitaxial grains was different. From the crystallization sequence, it is concluded that the initial crystallization of the metastable fluorite phase selectively *promotes* the perovskite epitaxy. In systems that directly transform into the final polycrystalline phase, elimination of grain boundary area is the only driving potential for the growth of the epitaxial film. In the case of the  $\text{PbTiO}_3$  epitaxy, the fluorite to perovskite transformation provides an *additional* driving potential for epitaxial growth. This phase transformation takes place over a narrow temperature range and it leads to textured  $\text{PbTiO}_3$  films at  $450^\circ\text{C}/1\text{h}$ , which is below its ferroelectric transformation temperature and at  $\sim 0.4$  of its melting temperature. As described above, a relatively small number of perovskite grains with the same orientation as of the substrate were observed to grow through to the film surface and consume the nano-crystalline, metastable fluorite phase. It appeared that this additional driving potential not only allows a few large grains to rapidly grow through the polycrystalline film, but also leads to entrapped porosity within the growing, epitaxial grains. Thus, the higher driving potential for converting the polycrystalline film of one phase into an epitaxial film of a second phase appears to be, in-part, responsible for entrapped porosity and the less ordered growth of the single crystal thin film.

#### 4.3 Film Densification, Mosaic Spread and Surface Pitting

The large mosaic spread in the initially crystallized perovskite phase cannot be attributed to mosaic spread in the STO substrate but rather must be a consequence of the growth process. Since the transforming perovskite grains are growing into a

partially dense polycrystalline fluorite matrix (which is also densifying during the phase transformation), it can be expected that each growing perovskite grain may be rotated, by a small amount, through differential densification. Differential densification of a powder matrix is common in composite systems and produces rotations of individual grains and groups of grains.<sup>50</sup> In the current case, the growing perovskite grains can be considered as the inclusions (or reinforcements) within the low density matrix.

The entrapped pores coarsen when the films are heat-treated at higher temperatures (Fig. 6b). After heating to temperatures in excess of 675°C/1h, the pores disappeared from within the epitaxied film and the surface becomes pitted (Fig. 7). Since pore disappearance requires material transport from the surface to the pore, or conversely, vacancy transport from the pore to the surface, it is obvious that the pits on the surface are the displaced pores from within the film. Heating to 800°C/1h ( $T \approx 0.69 T_{\text{melting}}$  of  $\text{PbTiO}_3$ ) is required to produce sufficient long-range surface mass-transport to form an epitaxial film with a smooth surface as shown in Figs. 8 and 9.

#### 4.4 Shear Strain Between Domains and Constraining Substrate

Although highly oriented  $\text{PbTiO}_3$  thin films were formed at 450°C/1h, below the Curie temperature of  $T_c \approx 490^\circ\text{C}$ , the growth of high quality epitaxial films required heat-treatments at 800°C/1h. Above  $T_c$ ,  $\text{PbTiO}_3$  has a cubic structure and it transforms to the tetragonal structure during cooling through  $T_c$ . At 800°C an in-plane, unrelaxed linear strain of  $\sim 1\%$  would exist between the  $\text{SrTiO}_3$  substrate and the cubic  $\text{PbTiO}_3$  phase. Misfit dislocations are generally assumed to accommodate much of this strain. The accommodation of mismatch strain by dislocations causes the film not to become strained to the cubic substrate lattice parameter  $a_{\text{STO}}$ , but rather to the 'effective substrate lattice parameter'  $a_{\text{STO}}^*$ , where  $a_{\text{STO}}^*$  is the substrate



lattice parameter,  $a_{\text{STO}}$ , modified by misfit dislocations as suggested by Speck and Pompe<sup>51</sup>. At 800°C, for cubic paraelectric  $\text{PbTiO}_3$  ( $a_{\text{PTO}} = 0.3975 \text{ nm}$ ) on cubic  $\text{SrTiO}_3$  ( $a_{\text{STO}} = 0.3938 \text{ nm}$ ),  $a_{\text{STO}}$  is smaller than  $a_{\text{PTO}}$  and it follows that  $a_{\text{STO}} < a_{\text{STO}}^* < a_{\text{PTO}}$ . Additional strain is produced during cooling through the Curie temperature when the paraelectric (cubic) structure transforms to the ferroelectric (tetragonal) structure. The relaxation of this additional strain occurs by the formation of *a*- and *c*-domains. Domain formation was first recognized by Roitburd<sup>52</sup> to be a means of strain relaxation in heteroepitaxial ferroelectric and ferroelastic films. In order to predict the stable domain configuration for a given substrate/film heteroepitaxial combination, Speck and Pompe<sup>51</sup> developed a temperature dependent domain stability map, incorporating the influence of i) lattice mismatch; ii) thermal expansion mismatch; iii) cooling rate; and iv) depolarizing fields. The schematic map for the dislocation free transformation for STO/PTO is shown in Fig. 12. It shows that with  $a_{\text{STO}} < a_{\text{PTO}}$  and  $a_{\text{STO}} < a_{\text{STO}}^* < a_{\text{PTO}}$  a mixed *c/a/c*-domain pattern can be expected as confirmed by the observations in the current study. A mixed domain structure should be favored due to the differential thermal expansion coefficient<sup>53</sup> ( $\alpha_{\text{PTO}} = 12.6 \times 10^{-6}/\text{K}$  above 490°C and  $\alpha_{\text{STO}} = 11 \times 10^{-6}/\text{K}$  (20°C - 1000°C)). Although no cooling rate experiments were conducted in this study, a high cooling rate of  $\sim 30^\circ\text{C}/\text{min}$  or higher can be expected,<sup>53</sup> and has been observed,<sup>9,11</sup> to enhance the formation of *c*-domains.

During the formation of *c*- and *a*-domains, the *c*-axis of the *c*-domains has to coherently fit to the *a*-axis in an *a*-domain. This is only possible if an equilibrium angle between the two domains is maintained. Using the room-temperature  $\text{PbTiO}_3$  *c/a* ratio, the angle is calculated to be  $3.55^\circ$ , provided that there are no constraints from the substrate.<sup>41</sup> As observed by SAD, HRTEM (Fig. 9) and in high resolution X-ray diffraction pole figures (Fig. 2), both *c*-domains and *a*-domains are rotated about  $\langle 100 \rangle_{\text{STO}}$  and  $\langle 010 \rangle_{\text{STO}}$ , away from the  $[001]_{\text{STO}}$  substrate normal. For

the epitaxial  $\text{PbTiO}_3$  films on  $\text{SrTiO}_3$ , the lattice match of the  $c$ -domains with the substrate is much better than for the  $a$ -domains ( $a_{\text{PTO}} = 0.3904$  nm,  $c_{\text{PTO}} = 0.4152$  nm,  $a_{\text{STO}} = 0.3905$ ; at room temperature). Because it is observed that the volume fraction of  $c$ -domains is larger than that of  $a$ -domains, it becomes a geometrical necessity to have small rotations on the order of  $\sim 0.7^\circ$  of the  $c$ -domains and larger rotations of  $\sim 2.2^\circ$  of the  $a$ -domains (Fig. 2; X-ray diffraction measurements were used here because TEM only samples a small area of the specimen). These results are described in detail by Daykin et al.<sup>41</sup> For both,  $c$ - and  $a$ -domains,  $\Omega$ -scans (Fig. 2b,d) showed the FWHM to be only about  $0.8^\circ$  and  $0.7^\circ$ , respectively.

## 5. Conclusions

A double-alkoxide liquid precursor was used to form epitaxial single crystal  $\text{PbTiO}_3$  thin films on  $\text{SrTiO}_3$ . Lead-loss during processing was successfully avoided by heating in a  $\text{PbO}$  containing atmosphere. Cross-section TEM showed that the formation of the epitaxial  $\text{PbTiO}_3$  thin films occurs through an intermediate polycrystalline  $\text{Pb-Ti-fluorite}$  phase. The concept of kinetically limited crystallization was applied to the formation of the metastable  $\text{Pb-Ti-fluorite}$  phase. Free energy considerations showed that the initial crystallization of the fluorite may be *advantageous* to obtain highly oriented  $\text{PbTiO}_3$  films at low temperatures ( $\sim 450^\circ\text{C}/1\text{h}$ ). However, initial fluorite formation may also encourage entrapped porosity, and thus lead to higher processing temperatures for formation of smooth, epitaxial films. A pattern of  $a$ - and  $c$ -domains was observed and their relative, small rotations about  $\langle 100 \rangle_{\text{STO}}$  and  $\langle 010 \rangle_{\text{STO}}$  were determined by TEM and X-ray diffraction.

### **Acknowledgments**

This work was supported by AFOSR under Contract No. 91-0125 and made use of MRL Central Facilities supported by the National Science Foundation under Award No. DMR-9123048. The authors also would like to thank Prof. M. Rühle and Susanne Stemmer of the Max-Planck Institute für Werkstoffwissenschaft, Stuttgart, for their support on some of the HRTEM work.

## References

1. L.M. Sheppard, Ceramic Bulletin, 71 (1), 85 (1992).
2. A.I. Kingon, *private communication*.
3. K. Iijima, R. Takayama, Y. Tomita, and I. Ueda, J. Appl. Phys., 60 (1), 2914 (1986).
4. E.V. Sviridov, V.A. Alyoshin, Y.I. Golovko, I.N. Zakharchenko, V.M. Mukhortov, and V.P. Dudkevich, phys. stat. sol. (a), 121, 157 (1990).
5. K. Iijima, I. Ueda, and K. Kugimiya, Jap. J. Appl. Phys., 30 (9b), 2149 (1991).
6. K. Kushida and H. Takeuchi, IEEE Transactions on Ultrasonics, Ferroelectrics, and Frequency Control, 38 (6), 656 (1991).
7. R. Bruchhaus, H. Huber, D Pitzer, and W. Wersing, Ferroelectrics, 127, 137 (1992).
8. J.T. Cheung, P.E.D. Morgan, and R. Neugaonkar, Integrated Ferroelectrics, 3, 147, (1993).
9. R. Ramesh, T. Sands, and V.G. Keramidas, Appl. Phys. Lett., 63 (6), 731 (1993).
10. R. Ramesh, H. Gilchrist, T. Sands, V.G. Keramidas, R. Haakenaasen, and D.K. Fork, Appl. Phys. Lett., 63 (26), 3592 (1993).

11. S. Matsubara, S. Miura, Y. Miyasaka, and N. Shohata, *J. Appl. Phys.*, **66** (12), 5826 (1989).
12. M. de Keijser, G.J.M. Dormans, J.F.M. Cillessen, D.M. de Leeuw, and H.W. Zandbergen, *Appl. Phys. Lett.*, **58** (23), 2636 (1991).
13. Y. Gao, G. Bai, K.L. Merkle, Y. Shi, H.L.M. Chang, Z. Shen, and D.J. Lam, *J. Mat. Res.*, **8** (1), 145 (1993).
14. J. Livage, M. Henry, and C. Sanchez, *Prog. Solid St. Chem.*, **18**, 259 (1988).
15. J.V. Mantese, A.L. Micheli, A.H. Hamdi, and R.W. West, *MRS Bul.* **14** (10), 48 (1989).
16. W. J. Daughton and S. L. Givens, *J. Electrochem. Soc.* **129** (1), 173 (1982).
17. C.J. Brinker and G. W. Scherer, *Sol-Gel Science*, Academic Press, NY 1990.
18. E.G. Bauer, B.W. Dodson, D.J. Ehrlich, L.C. Feldman, C.P. Flynn, M.W. Geis, J.P. Harbison, R.J. Matyi, P.S. Peercy, P.M. Petroff, J.M. Phillips, G.B. Stringfellow, and A. Zangwill, *J. Mat. Res.* **5** (4), 852 (1990).
19. F.F. Lange in *Proc. Recrystallization '92*, edited by M. Fuentes and J.G. Sevillano, Trans Tech Publications, Brookfield, VT, 81 (1992).
20. K. T. Miller, C.-J. Chan, M.G. Cain, and F. F. Lange, *J. Mat. Res.* **8** (1), 169 (1993). ?

21. A. Seifert, F.F. Lange, J.S. Speck, J. Am. Cer. Soc., 76 (2), 443 (1993).
22. K.T. Miller and F.F. Lange, J. Mat. Res. 6 (11), 2387 (1991).
23. K. Vaidya, C.Y. Yang, M. de Graef, and F.F. Lange, J. Mat. Res. 9 (5), 410 (1994).
24. S.J. Golden, F.F. Lange, D.R. Clarke, L.D. Chang, and C.T. Necker, Appl. Phys. Lett., 61, 351 (1992).
25. C.K. Barlingay and S.K. Dey, Appl. Phys. Lett., 61 (11), 1278 (1992).
26. S.L. Swartz, S.D. Ramamurthi, J.R. Busch, and V.E. Wood in *Mat. Res. Soc. Proc.*, 243, *Ferroelectric Thin films II*, MRS Pittsburgh, PA, 533 (1992).
27. S. Hirano, T. Yogo, K. Kikuta, Y. Araki, M. Saitoh, and S. Ogasahara, J. Am. Cer. Soc., 75 (10), 2785 (1992).
28. B.A. Tuttle, J.A. Voigt, D.C. Goodnow, D.L. Lamppa, T.J. Headley, M.O. Eatough, G. Zender, R.D. Nasby, and S.M. Rodgers, J. Am. Cer. Soc., 76 (6), 1537 (1993).
29. D.S. Yoon, C.J. Kim, J.S. Lee, W.J. Lee, and K. No, J. Mat. Res. 9 (2), 420 (1994).
30. J.B. Blum and S.R. Gurkovich, J. Mater. Sci, 20, 4479 (1985).
31. A.P. Wilkinson, J.S. Speck, A.K. Cheetham, S. Natarajan, and J.M. Thomas, Chem. Mater., 6 (6), 750 (1994).

32. C.K. Kwok, S.B. Desu, and L. Kammerdiner in *Mat. Res. Soc. Proc.*, 200, *Ferroelectric Thin films*, MRS Pittsburgh, PA, 83 (1990).
33. A.H. Carim, B.A. Tuttle, D.H. Doughty, and S.L. Martinez, *J. Am. Cer. Soc.*, 74 (6), 1455 (1991).
34. B.A. Tuttle, R.W. Schwartz, D.H. Doughty, and J.A. Voigt in *Mat. Res. Soc. Proc.*, 200, *Ferroelectric Thin films*, MRS Pittsburgh, PA, 159 (1990).
35. J.F. Chang and S.B. Desu, *J. Mat. Res.* 9 (4), 955 (1994).
36. S.R. Gurkovich and J.B. Blum in *Ultrastructure Processing of Ceramics, Glasses and Composites*, edited by L.L. Hench and D.R. Ulrich, Wiley-Interscience, NY, 152 (1984).
37. S.D. Ramamurthi and D.A. Payne, *J. Am. Cer. Soc.*, 73 (8), 2547 (1990).
38. K.D. Budd, S.K. Dey, and D.A. Payne, *Proc. Br. Ceram. Soc.*, 36, 107 (1985).
39. G. Shirane, R. Pepinsky, and B.C. Frazer, *Acta. Cryst.*, 9, 131 (1956).
40. R. LeBihan, *Ferroelectrics*, 97, 19 (1989).
41. A.C. Daykin, A. Seifert, W. Pompe, and J.S. Speck, to be published
42. D.K. Leung, C.J. Chang, M. Ruehle, and F.F. Lange, *J. Am. Cer. Soc.*, 74 (11), 2786 (1991).

43. M.L. Balmer, F.F. Lange, and C.G. Levi, *J. Am. Cer. Soc.*, **75** (4), 946 (1992).
44. T. Tani and D.A. Payne, *J. Am. Cer. Soc.*, **77** (5), 1242 (1994).
45. M.A. Subramanian, G. Aravamudan and G.V.S. Rao, *Prog. Solid St. Chem.*, **15**, 55 (1983).
46. V. Jayaram, M De Graef, and C.G. Levi, *Acta Met. et Mat.*, **42** (6), 1829 (1994).
47. R.L. Holman and R.M. Fulrath, *J. Appl. Phys.*, **44** (12), 5227 (1973).
48. O. Yamaguchi, T. Fukuoka, and Y. Kawakami, *J. Mater. Sci. Lett.*, **9**, 958 (1990).
49. H. Hu, C.J. Peng, and S.B. Krupanidhi, *Thin Solid Films*, **223**, 327 (1993).
50. O. Sudre and F.F. Lange, *J. Am. Cer. Soc.*, **75** (3), 519 (1992).
51. J.S. Speck and W. Pompe, to be published in *J. Appl. Phys.*, (1994).
52. A.L. Roitburd, *Phys. Stat. Sol. (a)*, **37**, 329 (1976 ).
53. J.S. Speck, A. Seifert, W. Pompe, and R. Ramesh, to be published in *J. Appl. Phys.*, (1994).



## Figure Captions

Fig. 1: X-ray diffraction  $\Theta$ - $\Theta$  scans on  $\text{PbTiO}_3$  thin films heated at different temperatures. The intensity of the (00 $l$ ) reflections increases strongly as the heat-treatment temperature is raised from 450°C/1h to 800°C/1h and indicates the development of epitaxy.

Fig. 2: a) High resolution pole figure scan on (002) of a  $\text{PbTiO}_3$  film heated at 800°C/1h. Four different  $c$ -domain orientations can be seen. The rotation about  $\langle 100 \rangle_{\text{STO}}$  and  $\langle 010 \rangle_{\text{STO}}$  is  $\sim 0.7^\circ$  from the substrate normal  $[001]_{\text{STO}}$ .

b) The  $\Omega$ -scan on the  $c$ -domains can be fit to two overlapping Gaussians. The FWHM of the individual Gaussians is  $\sim 0.9^\circ$  and  $\sim 0.8^\circ$ , respectively.

c) High resolution pole figure scan on (200) of the  $\text{PbTiO}_3$  film. Four different  $a$ -domain orientations can be seen. The rotation about  $\langle 100 \rangle_{\text{STO}}$  and  $\langle 010 \rangle_{\text{STO}}$  is  $\sim 2.2^\circ$  from the substrate normal  $[001]_{\text{STO}}$ .

d)  $\Omega$ -scan on one of the  $a$ -domain orientations at  $\psi = -0.3^\circ$  and  $\Delta \omega = 2.2^\circ$ . The FWHM for the  $a$ -domains is  $\sim 0.7^\circ$ .

Fig. 3: SEM on films heated at different temperatures (see X-ray diffraction in Fig. 1). A nanocrystalline film at 425°C/1h (a) coarsens and densifies as seen at 625°C/1h (b). Faceting at 675°C/1h (c) indicates epitaxy and at 800°C/1h (d) a smooth film surface showing ferroelectric domains that are imaged by voltage contrast.

Fig. 4: a) BF TEM of a film heated at  $\sim 380^\circ\text{C}/1\text{h}$ . Nucleation of a Pb-Ti-phase with a fluorite structure (see 4b) with  $a=0.49\text{ nm}$ . The inset SAD pattern shows an amorphous ring from the matrix as well as reflections from the Pb-Ti-fluorite.

b) SAD of the film at  $\sim 400^\circ\text{C}/1\text{h}$  showing that the film consists primarily of the polycrystalline Pb-Ti-fluorite.

Fig. 5: a) BF TEM of a film heated at  $\sim 420^\circ\text{C}/1\text{h}$ . Starting at the interface, polycrystalline Pb-Ti-fluorite transforms into a highly {001} textured tetragonal perovskite that consumptively grows through the fluorite to the film surface.

b) SAD and DF TEM with the (020)-substrate/film reflection shows that the tetragonal perovskite is highly {001} textured with a large mosaic spread.

Fig. 6: a) BF TEM. At  $650^\circ\text{C}/1\text{h}$  the film has undergone significant coarsening and concurrent decrease of mosaic spread (see inset SAD pattern). Ferroelectric domains as well as residual pores can be seen in the film.

b) DF TEM using a substrate/film reflection showing completion of oriented layer formation.

Fig. 7: BF TEM image of a completely epitaxial, faceted film of a specimen heated at  $675^\circ\text{C}/1\text{h}$ . As suggested by SEM, large residual grains of similar orientation (TEM) remain at the film surface.

Fig. 8: At  $800^\circ\text{C}/1\text{h}$  the surface has become smooth by evaporation/condensation or surface diffusion. The film has a low threading dislocation density and shows strain contrast from disclinations at the domain-boundary/interface intersections and misfit dislocations in *c*-domains.

Fig. 9: HRTEM image of the film in Fig. 8, heated at  $800^\circ\text{C}/1\text{h}$ . Narrow *a*-domains (*c* || interface) and wide *c*-domains (*c*  $\perp$  interface) can be seen. The

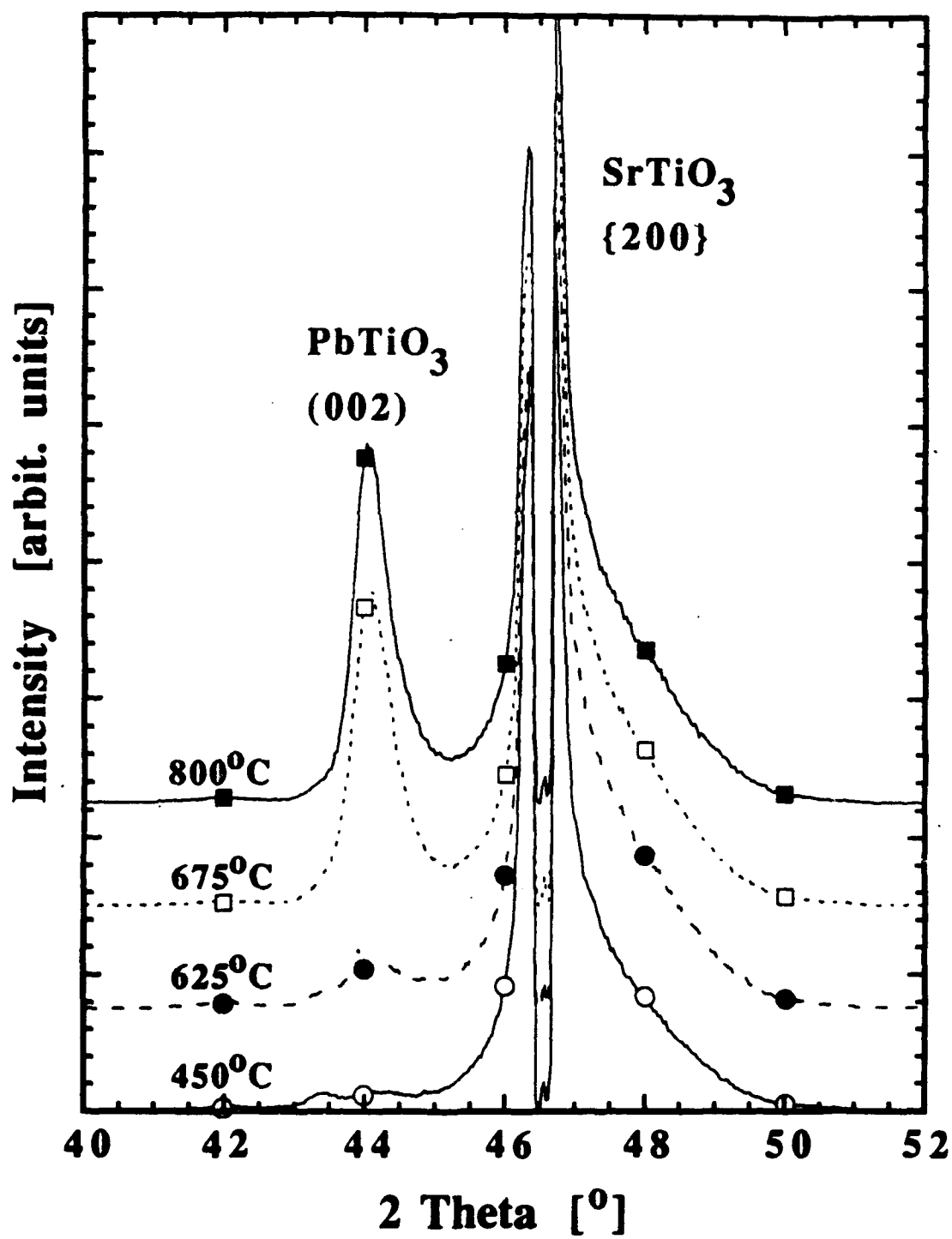
twinning angle between *a*- and *c*-domains as well as the resulting change in surface orientation can be observed.

Fig. 10: AFM on the film heated at 800°C/1h allows to image the ferroelectric domain structure due to the change in surface orientation as a result of twinning.

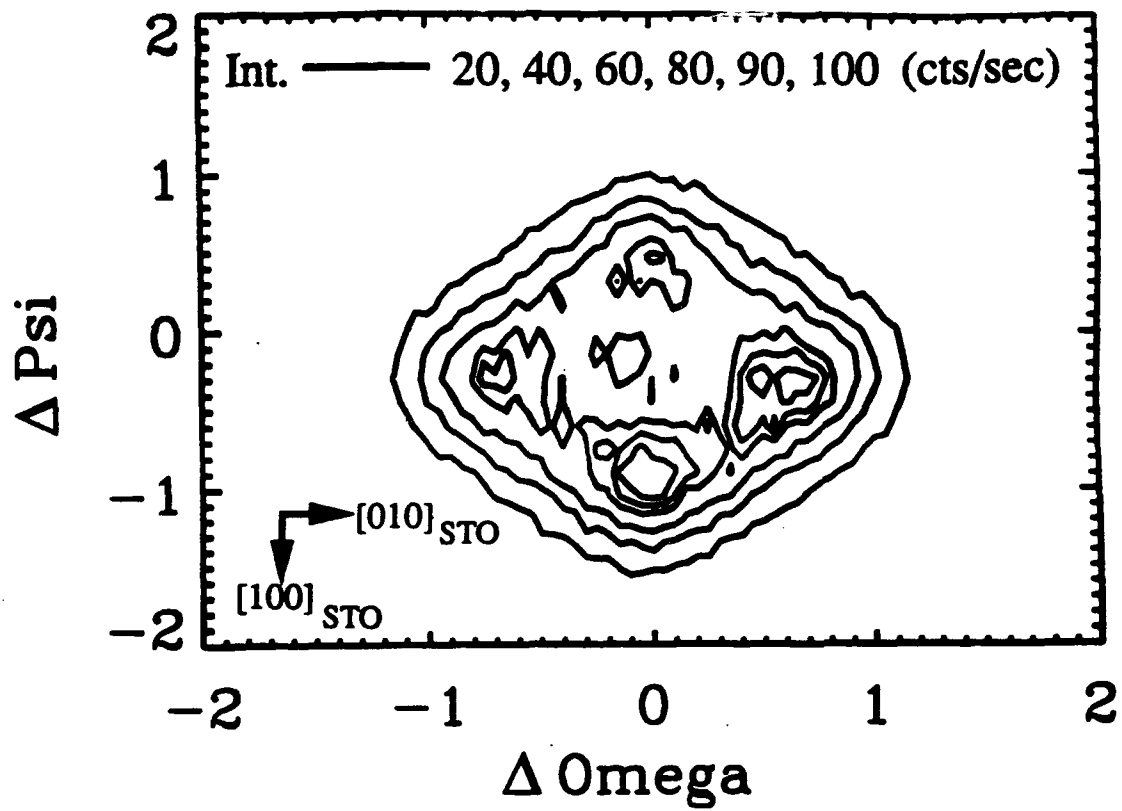
Fig. 11: Schematic free energy diagram of the system PbO-TiO<sub>2</sub> showing the relative free energy curves for the amorphous precursor, fluorite, and perovskite phases. Path 1 gives the crystallization sequence for a stoichiometric precursor and Path 2 illustrates the sequence for a non-stoichiometric composition.

Fig. 12: Coherent domain stability map for SrTiO<sub>3</sub>/PbTiO<sub>3</sub>. It shows that with  $a_{\text{STO}} < a_{\text{PTO}}$  and  $a_{\text{STO}} < a_{\text{STO}}^* < a_{\text{PTO}}$ , a *c/a/c*-domain pattern can be expected.<sup>51</sup>

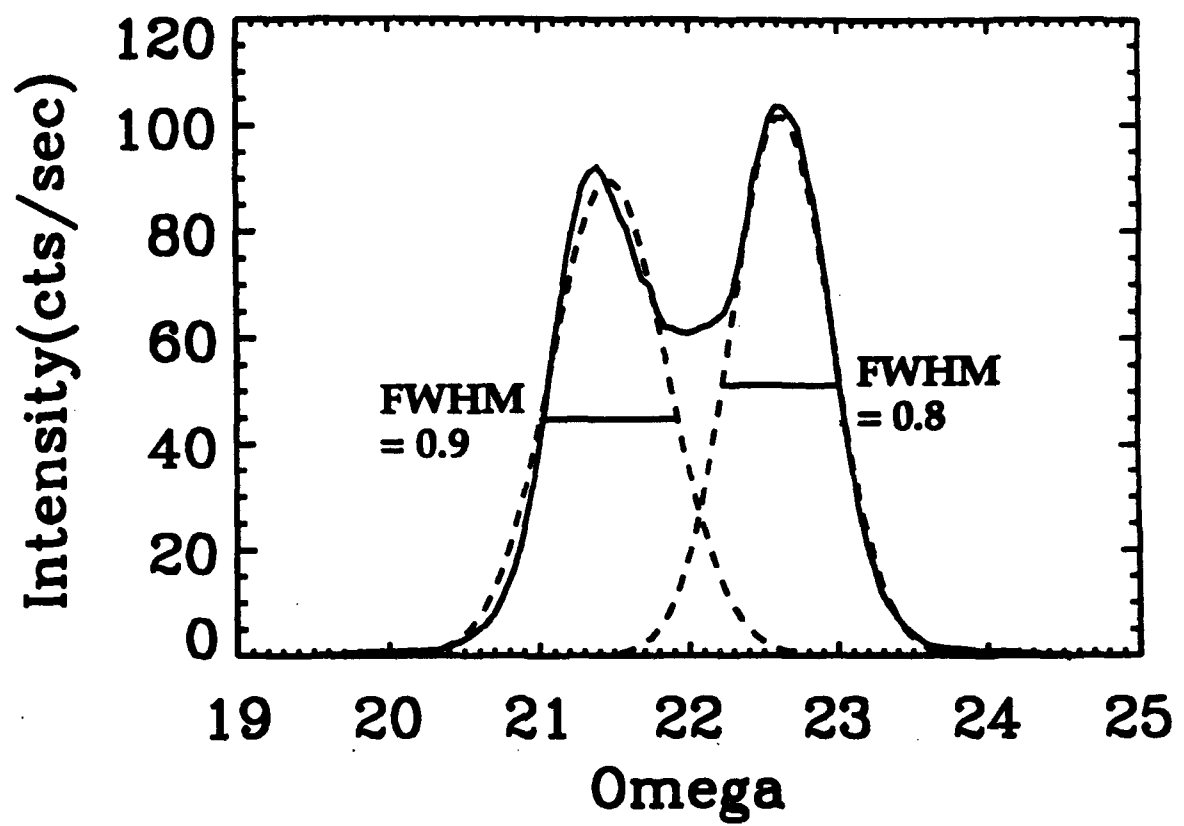
## X-ray Data for $\text{PbTiO}_3$ Thin Films



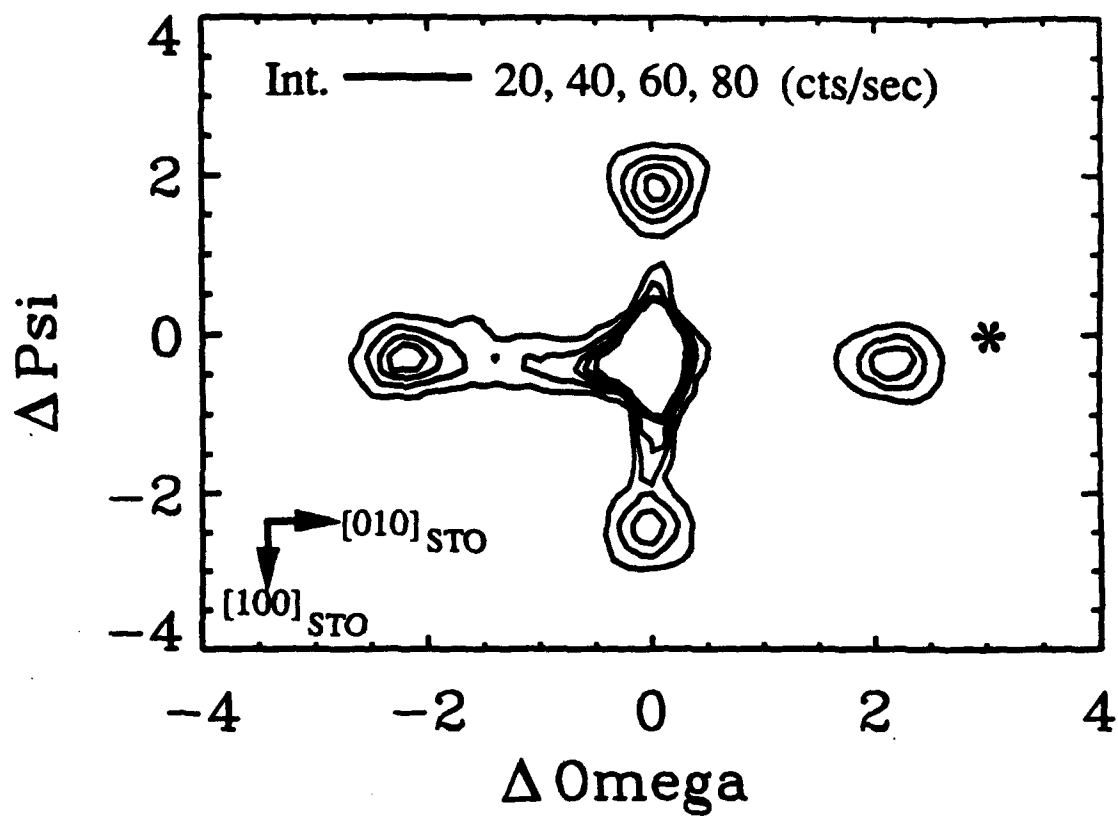
# c-domains



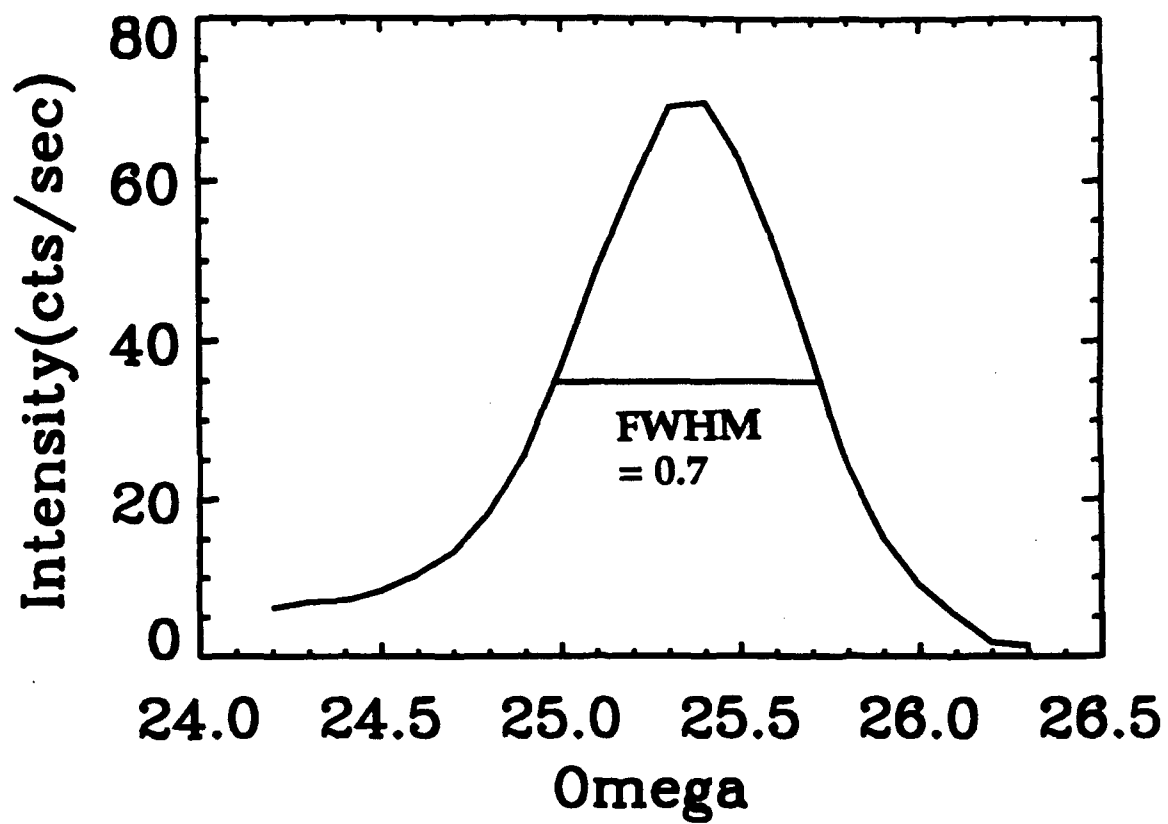
# c-domains



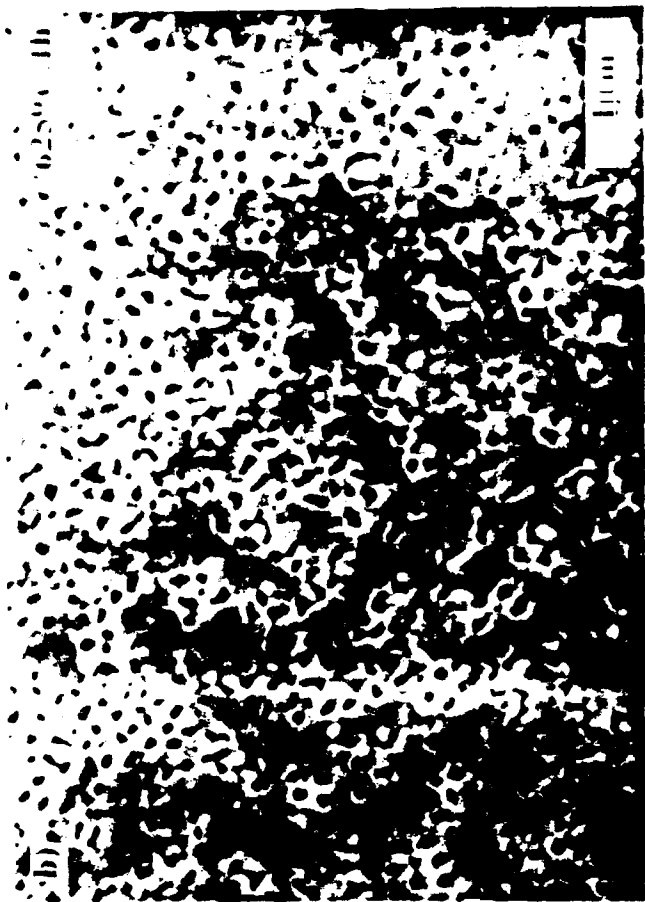
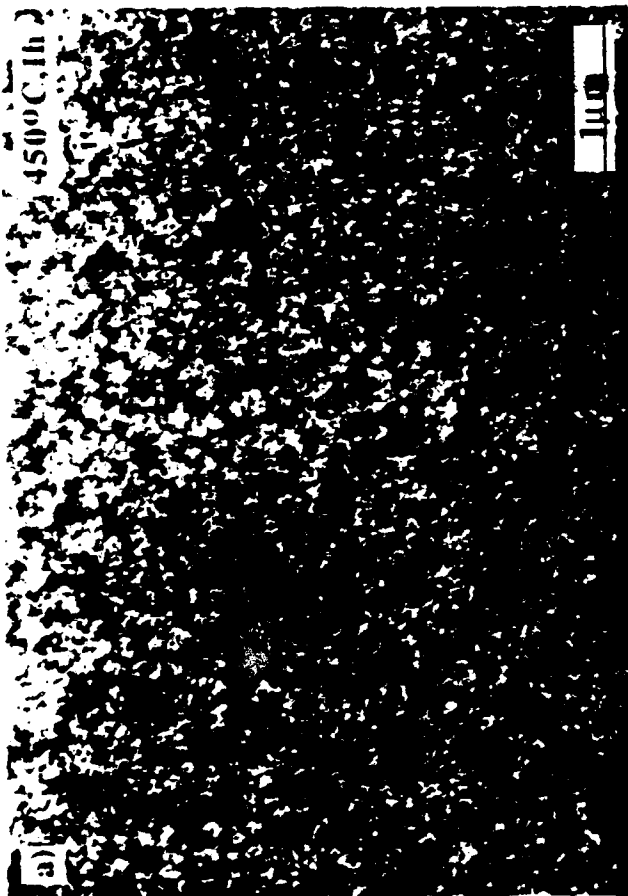
# a-domains



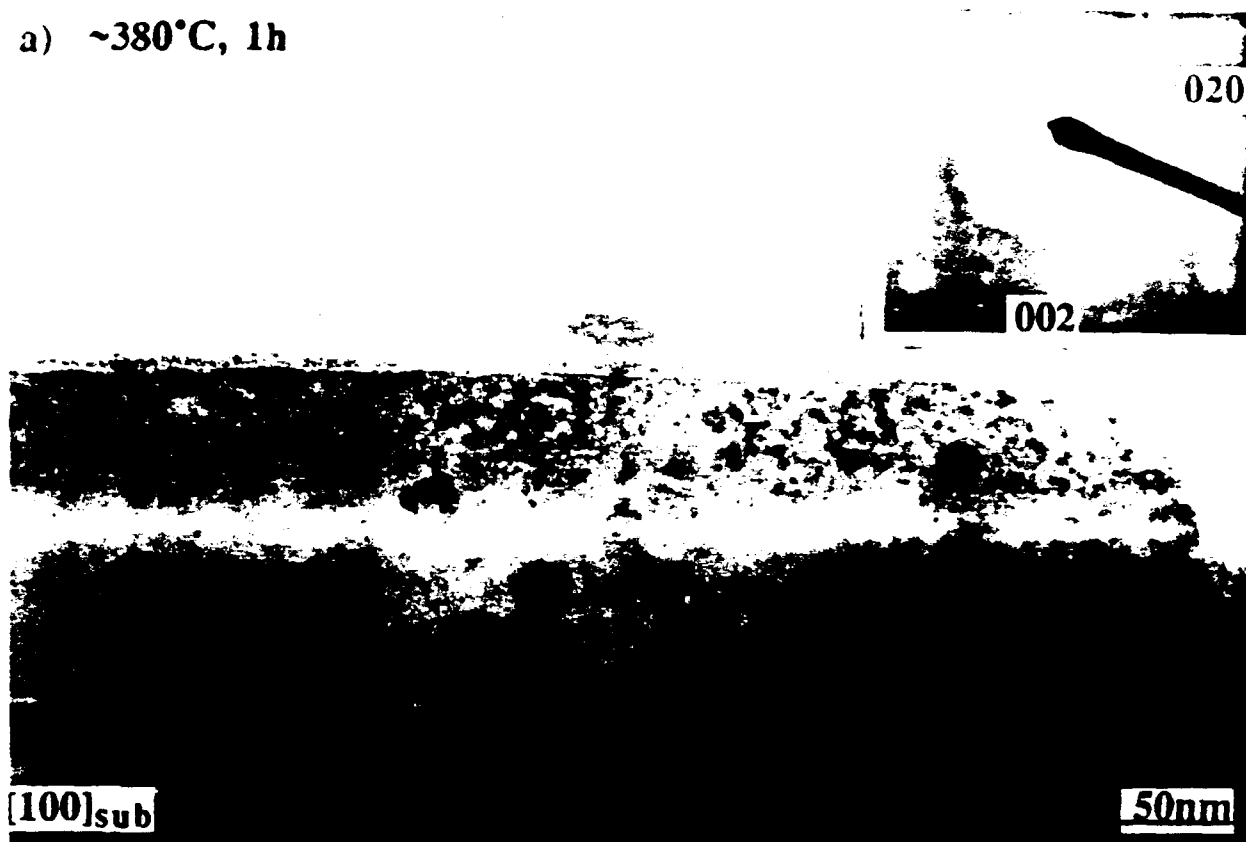
a-domain at \*

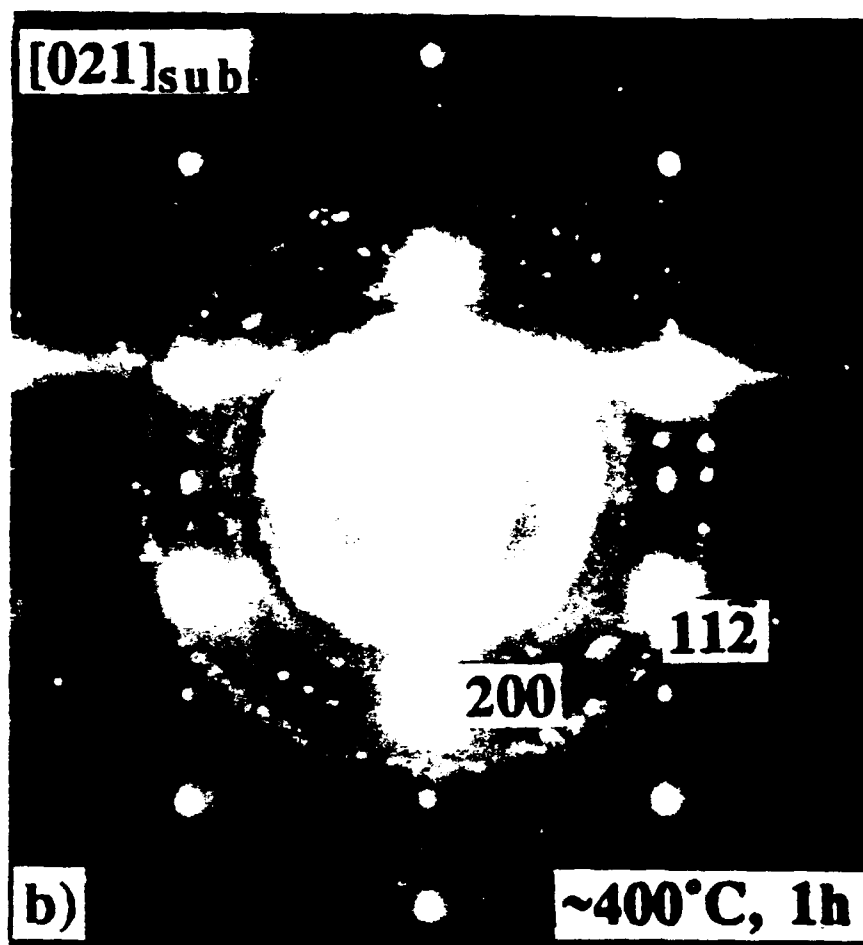


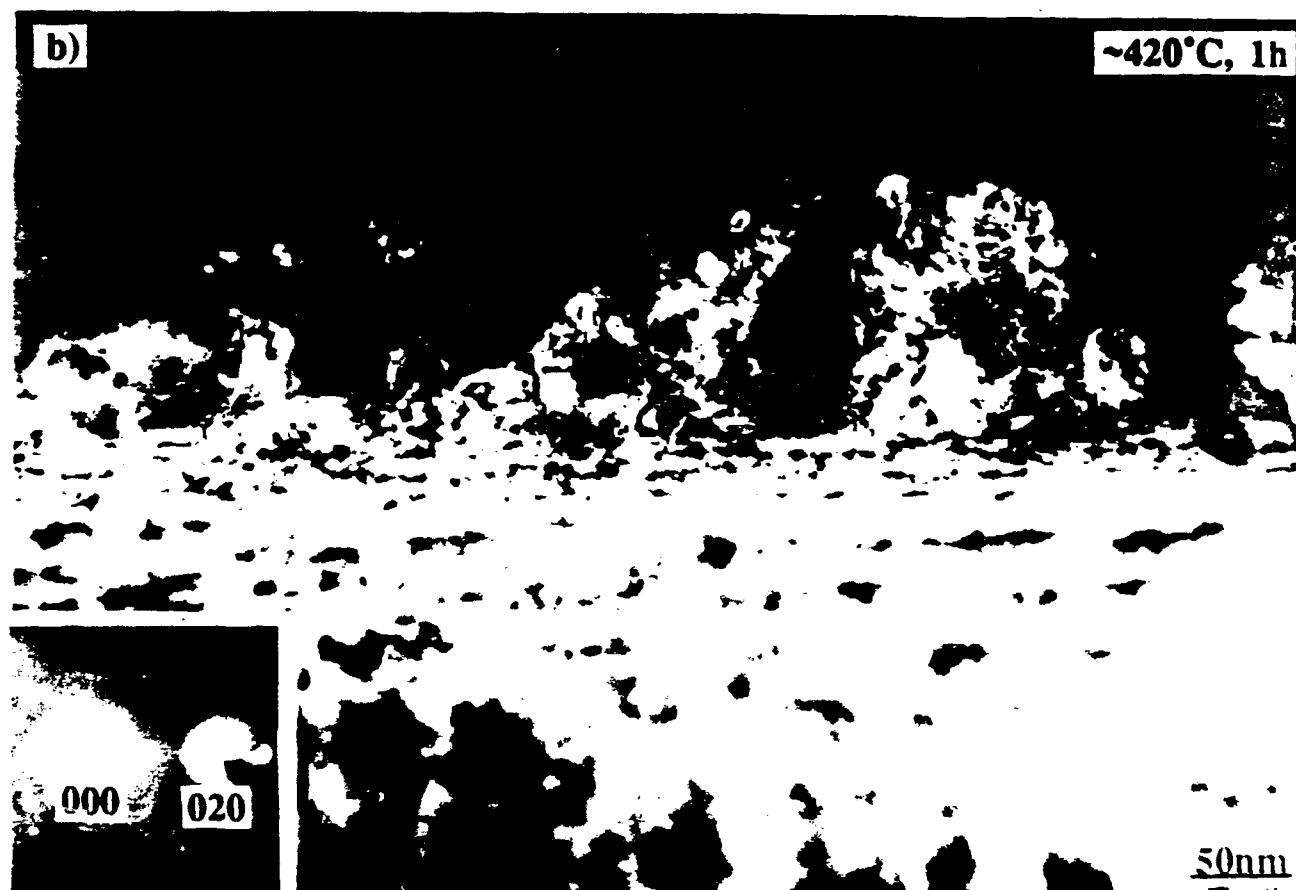




a)  $\sim 380^{\circ}\text{C}$ , 1h

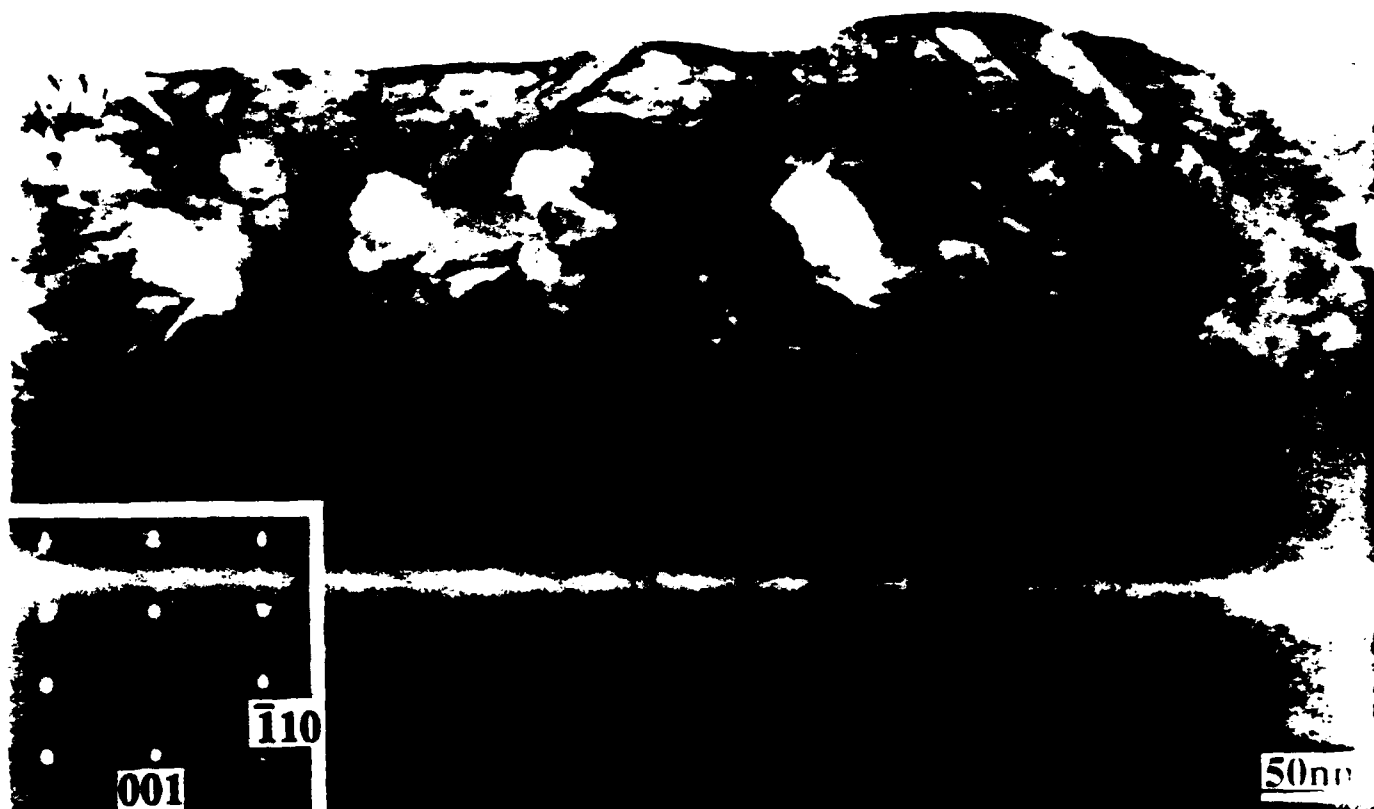






10 [110]

650°C



b)

650°C



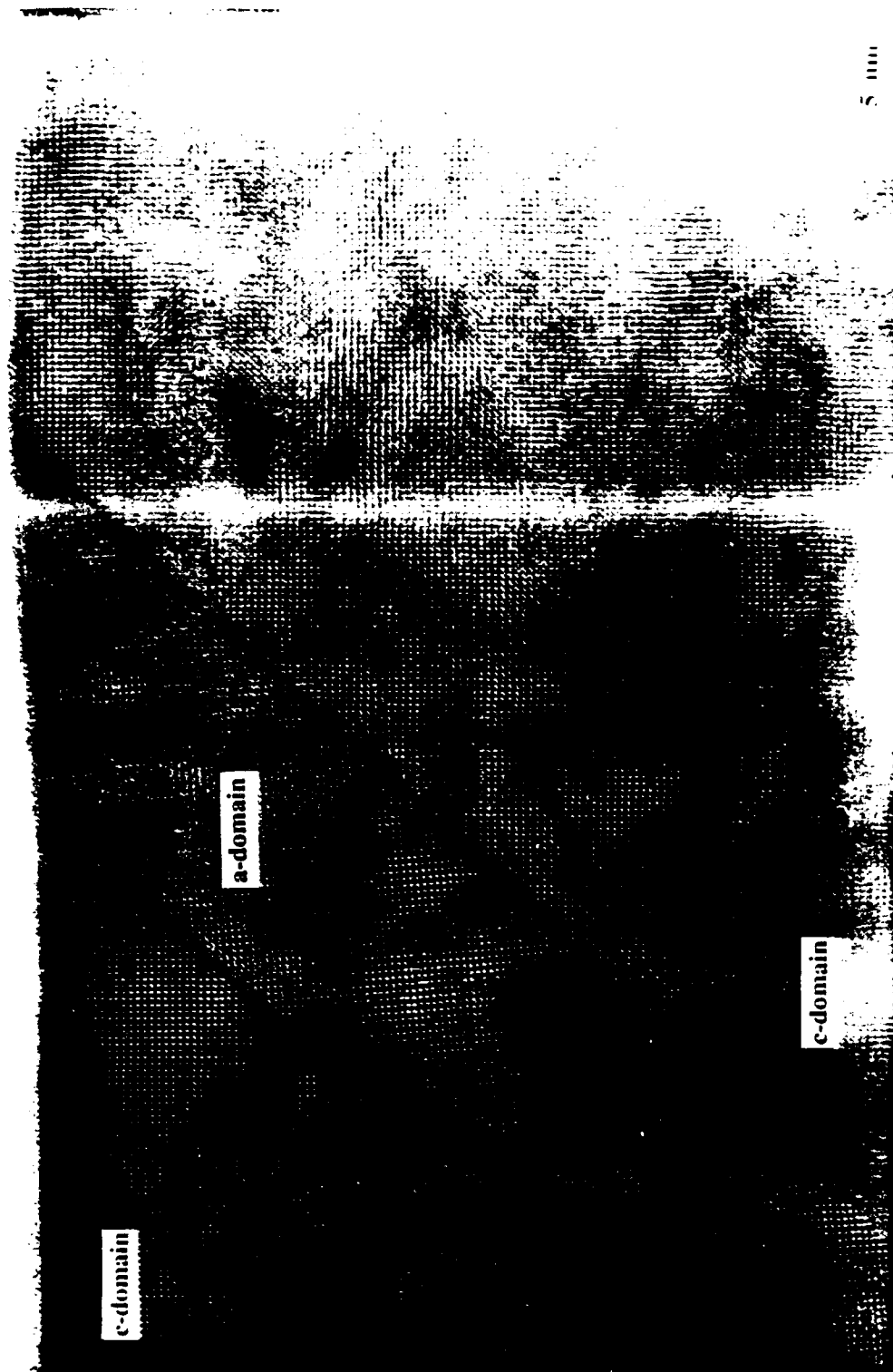
675°C.1h





8000C, 1h

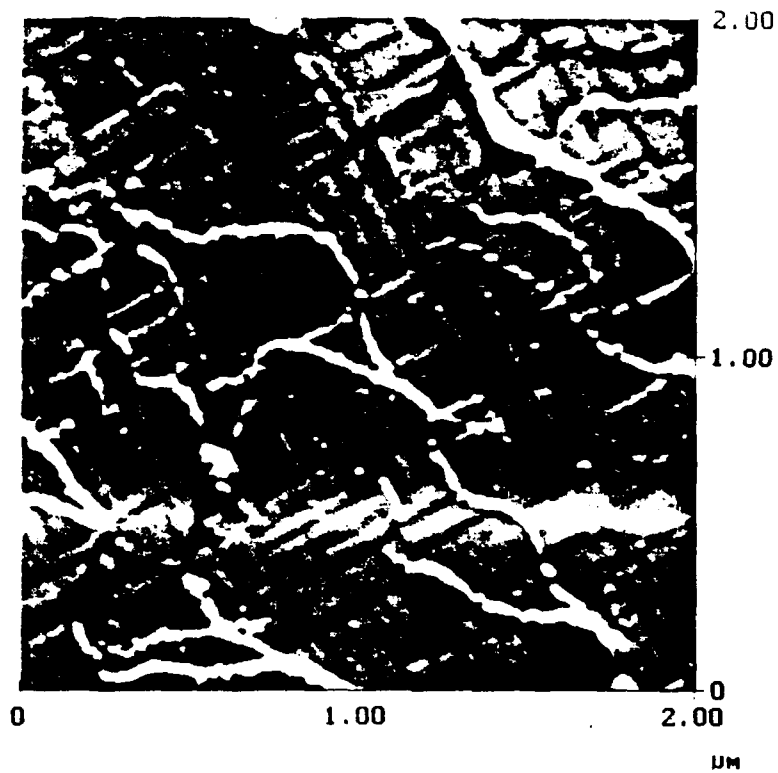
[100]



500 nm



PbTiO<sub>3</sub> on (100) SrTiO<sub>3</sub> - 800 °C, 1h



Height

5.0 nm

2.5 nm

0.0 nm

AFM

